Chemically induced compaction bands: Triggering conditions and band thickness

Ioannis Stefanou, Jean Sulem

Chemically induced compaction bands: Triggering conditions and band thickness

Ioannis Stefanou and Jean Sulem

Université Paris-Est, Laboratoire Navier, CNRS (UMR 8205), ENPC, IFSTTAR

Corresponding author: I.Stefanou, Ecole Nationale des Ponts et Chaussées, 77455 Marne la Vallée, Cedex 2, France, (ioannis.stefanou@enpc.fr)

Key points

- Compaction band instabilities due to cataclasis and dissolution in rocks
- Strong chemo-poro-mechanical coupling, grain breakage and chemical softening
- Regions of instability, compaction band thickness and periodicity

Abstract

During compaction band formation various mechanisms can be involved at different scales. Mechanical and chemical degradation of the solid skeleton and grain damage are important factors that may trigger instabilities in the form of compaction bands. Here we explore the conditions of compaction band formation in quartz- and carbonate-based geomaterials by considering the effect of chemical dissolution and grain breakage. As the stresses/deformations evolve, the grains of the material break leading to an increase of their specific surface. Consequently, their dissolution is accelerated and chemical softening is triggered. By accounting for (a) the mass diffusion of the system, (b) a macroscopic failure criterion with dissolution softening and (c) the reaction kinetics at the micro level, a model is proposed and the conditions for compaction instabilities are investigated. Distinguishing the micro-scale (grain level) from the macro-level (Representative Elementary Volume) and considering the heterogeneous microstructure of the REV it is possible to discuss the thickness and periodicity of compaction bands. Two case studies are investigated. The first one concerns a sandstone rock reservoir which is water flooded and the second one a carbonate rock in which CO_2 is injected for storage. It is shown that compaction band instabilities are possible in both cases. (200 words)

Index terms

STRUCTURAL GEOLOGY: Mechanics, theory and modeling

NONLINEAR GEOPHYSICS: Bifurcations and attractors, Critical phenomena, Pattern formation
COMPUTATIONAL GEOPHYSICS: Modeling

Keywords
Compaction band instabilities, Strain localization, Chemo-poro-mechanical coupling, Grain breakage, Rocks, Reservoirs

1. Introduction

The presence of compaction bands in nature may provide useful information on various geological processes as it is an indication of the stress state history of a geological formation. Compaction bands are usually characterized by a significant reduction of the pore space, which in most of the cases is accompanied by an important reduction in permeability. Thus, compaction bands are also important in reservoir mechanics for oil production and CO_2 storage [*Olsson et al.*, 2002; *Holcomb et al.*, 2007; *Rutqvist*, 2012]. Pore collapse, intergranular grain fracturing and sliding, Hertzian cracking at grain contacts, grain crushing, grain attrition, grain-matrix debonding and matrix fracturing are often observed to a less or bigger extent inside the compacting zone [*Baud et al.*, 2004, 2009; *Sternlof et al.*, 2005; *Tondi et al.*, 2006; *Holcomb et al.*, 2007; *Aydin and Ahmadov*, 2009; *Zhu et al.*, 2010; *Cilona et al.*, 2012; *Rustichelli et al.*, 2012; *Wong and Baud*, 2012]. In parallel, it has been observed that reactive fluids play a significant role in creep and compaction of porous rocks [e.g. *Le Guen et al.*, 2007; *Liteanu and Spiers*, 2009; *Rutqvist*, 2012]. Generally, mechanical damage and chemical degradation of the solid skeleton (i.e. of the grains and matrix) are important factors that may trigger instabilities in the form of compaction bands. The objective of the present paper is to explore the possibilities and conditions of compaction band formation due to chemo-mechanical reasons in porous geomaterials.

In the frame of Continuum Mechanics, compaction bands can be seen as an instability of the underlying mathematical problem. Discrete approaches like the Discrete Element Method have also been proposed in the literature [*Katsman et al.*, 2005; *Katsman and Aharonov*, 2006; *Wang et al.*, 2008; *Marketos and Bolton*, 2009, among others] but they are computationally intensive and the identification of the general conditions that lead to strain localization is not straightforward. On the other hand a continuum approach can reveal the conditions for compaction band triggering given the constitutive behavior of the material [*Rudnicki and Rice*, 1975; *Vardoulakis and Sulem*, 1995; *Rudnicki*, 2002]. It is commonly observed that strain localization is favored by strain softening and most of the existing theoretical studies focus on pure mechanical reasons for compaction band formation (mechanical softening due to grain and matrix damage and pore collapse). Nevertheless, more recently, the role of chemical softening on

slip instabilities has been explored [e.g. *Brantut and Sulem*, 2012; *Veveakis et al.*, 2012, 2013] showing that chemistry may play an important role in shear band instabilities and strain localization. Here we focus on the conditions that lead to the formation of pure compaction bands in quartz- or carbonate-based geomaterials by considering the effect of chemical dissolution. Shear enhanced compaction bands are out of the scope of the present study and their investigation can be a future extension of the proposed model.

The effect of chemical dissolution is important in field and in reservoir applications. For instance, the experimental results of Xie et al. [2011] showed that the chemical dissolution of a limestone leads to a significant increase of the porosity (from 23% for the intact rock to 27% for the degraded one). According to the same authors, the plastic pore collapse threshold is also reduced from about 30 to 20 MPa and the chemically degraded materials become more collapsible and more ductile due to the increase in porosity and the degradation of the inter-granular cementation. This evidence is corroborated by other authors [e.g. *Nova et al.*, 2003; *Hu and Hueckel*, 2007b; *Zinsmeister et al.*, 2013] for a class of geomaterials and results in a contraction of the elastic domain only due to chemical reasons (chemical softening). In parallel, in a saturated porous geomaterial, the progressive mechanical damage of the solid skeleton during compaction has as a result the increase of the interface area of the reactants (i.e. of the solution with the solid) and consequently the acceleration of the dissolution rate of the solid phase [cf. *Rimstidt and Barnes*, 1980]. Thus, the solid skeleton is degraded more rapidly (mass removal because of dissolution), the overall mechanical properties of the system diminish (contraction of the elastic domain – chemical softening), deformations increase and the solid skeleton is further damaged (intergranular fractures, debonding, breakage of the porous network etc.). Figure 1 schematically shows this positive feedback process, whose stability is not guaranteed. Actually, as it will be shown in this paper, instabilities in the form of compaction bands may be triggered.

The impact of chemical phenomena and, in particular, of pressure solution inside deformation bands, has been demonstrated in several cases [*Tondi et al.*, 2006; *Tondi*, 2007; *Liteanu and Spiers*, 2009; *Cilona et al.*, 2012; *Rustichelli et al.*, 2012]. However, the effect of dissolution on compaction band formation is difficult to observe in the field and its exact role is still a subject of investigation. Notice that field observations are made long after the formation of compaction

bands, where the poro-mechanical properties of the rock have obviously drastically changed. Exploring the effects of dissolution prior to compaction band formation is also a difficult task in the laboratory as the reproduction of the field conditions is not straightforward. Nevertheless, recent experimental tests with dissolvable surrogate materials and numerical studies with the Discrete Element Method have shown that dissolution of grains causes pronounced changes in the fabric and in the intergranular force transmission that may result in episodic microstructural changes and to strain localization [*Shin*, 2009; *Shin and Santamarina*, 2009; *Tran et al.*, 2012]. The aforementioned indications of chemically induced strain localization instabilities provides the motivation of the present study and justifies the consideration of strong chemo-mechanical couplings in models due to dissolution.

Two scales are distinguished in the present chemo-hydro-mechanical model. The first scale is related to the macroscopic poromechanical behavior of the geomaterial. At this level the mass balance equation and the stress equilibrium are expressed over the representative elementary volume (REV). The second scale, which will be called here micro-scale, concerns the behavior of a single grain of the geomaterial and its surrounding matrix. Intergranular and matrix fracturing, grain-matrix debonding and the dissolution reaction kinetics refer to this scale. The distinction of the micro- and the macro-scale is presented schematically in Figure 2. The bridging between the macro- and the micro-scale is achieved here through the empirical law of Lade [1996], which relates the effective grain size to the mechanical energy input to the system. In this sense, at least part of the mechanical energy is dissipated through the various micro-mechanisms related to the solid skeleton damage for the creation of new surfaces in the medium (fracturing). The advantage of the aforementioned empirical law over other micromechanical approaches is that it needs the calibration of only one parameter. More sophisticated grain damage models that account for the degradation of the inter-granular cement of rocks might be suitable, but the chosen phenomenological approach is a first step for studying some key features of chemical degradation on compaction banding by avoiding unnecessary complexity. Dissolution reaction kinetics at the micro-level (i.e. at the scale of a single grain) are then up-scaled to the macro-level.

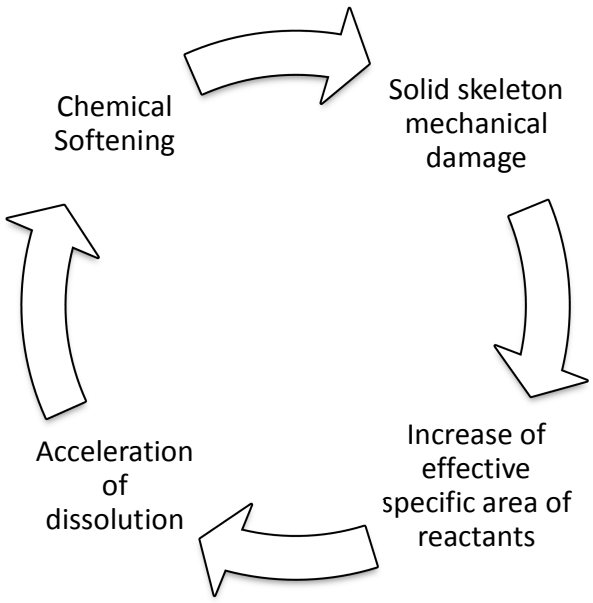

Figure 1. Positive feedback process due to dissolution and solid skeleton damage (e.g. intergranular fracturing, breakage of the porous network, matrix cracking, grain-matrix debonding etc.)

As it was already mentioned, the present analysis aims at exploring the possibilities of compaction band formation due to chemical softening effects only. Therefore, mechanical softening (or hardening) induced by grain damage or pore collapse is not considered herein in order to isolate the chemical effects. This means that the effect of grain damage and pore collapse on the evolution of the yield surface as described for instance by Das et al. [2011] is neglected. On the other hand the effect of the damage of the solid skeleton on the acceleration of chemical reaction is taken into account by explicitly introducing the effective specific surface of the grains in the reaction kinetics law. Of course it is possible to account also for mechanical softening/hardening due to grain damage and pore collapse but this would somewhat hide the role of chemical effects explored here.

The first two sections of the paper are devoted to the formulation of the proposed chemo-poro-mechanical model by distinguishing the micro- and the macro-level behavior. At the macro-level (section 2), the constitutive behavior of the material is described within the frame of plasticity theory, the mass balance equation is derived and the linear momentum balance is set forth in

order to account for the different species in the REV. At the micro-level (section 3), the evolution of the effective grain size due to various micro mechanisms is described and the reaction kinetics are formulated and upscaled to the macro-level. Next, in section 4, the possibility of compaction band formation is discussed through a linear stability analysis. A criterion for compaction band instabilities is proposed and its sensitivity to the various parameters of the model is explored. Note that because of the strong chemo-poro-mechanical coupling, the application of the classical localization criterion of Rice [1976] is not straightforward. Finally, in section 5 two examples of compaction band instabilities are given for a quartzic rock under water flooding conditions and for a carbonate grainstone in relation with CO_2 injection and storage. All the mathematical calculations were performed with the symbolic language mathematical package Mathematica© and they are available to the reader upon request.

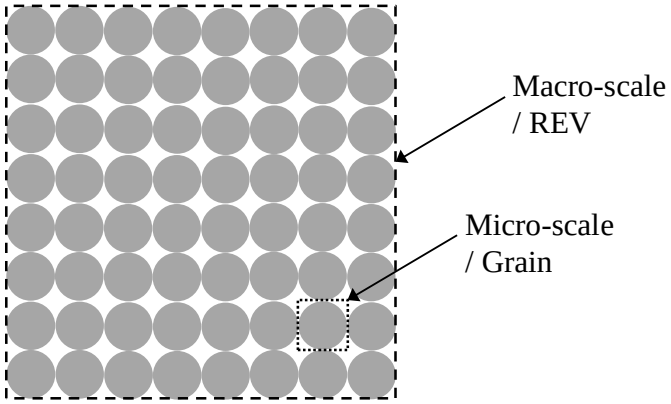

Figure 2. Schematic representation of the REV (macro-scale) and of the grains (micro-scale). The picture is an idealization of the microstructure of a rock. The dissolution rate is homogeneous in the REV when the size and the chemical composition of the grains is homogeneous. In the case of compaction bands, the grains break, their size is not necessarily uniform in the REV and consequently the dissolution rate is not any more homogeneous.

2. Macro-scale

2.1. Constitutive behavior

Based on experimental research and theoretical considerations, several constitutive laws have been proposed in the literature that relate the observed macroscopic stresses and strains. Plasticity

143 theory is a standard framework for the mathematical formulation of the underlying mechanical
144 problem. For a recent review of common plasticity models used for porous rocks we refer to
145 Wong and Baud [2012].
146
147 Depending on the applied stress path, the boundary conditions and the geomaterial at hand, a
148 strain hardening or softening response can be observed due to the various mechanisms, which
149 take place at the microlevel, i.e. at the grain-scale, and are related to the evolution of the
150 microstructure of the solid skeleton (e.g. pore collapse) and to grain damage (e.g. grain
151 fracturing). However, for the reasons exposed in the introduction, only chemical softening will be
152 considered herein.
153
154 The removal of minerals from the solid skeleton through chemical processes causes the
155 mechanical strength of the rock to decrease [e.g. *Hu and Hueckel*, 2007a, 2007b]. Therefore, we
156 expect the mechanical strength of a rock to be a function of the (residual) mass of the solid
157 skeleton after the dissolution process. Expressing as $\zeta = \zeta(t) = \dfrac{M_s(t)}{M_s^0}$, $0 \le \zeta \le 1$, the ratio of the
158 current mass, $M_s(t)$, of the constituent 's' over its initial mass, $M_s^0 = M_s(t=0)$, in the REV
159 before the chemical process starts (initial/reference state), ζ can be seen as a chemical softening
160 parameter [see also Nova et al., 2003; Hu and Hueckel, 2007b]. Assuming compression negative,
161 Figure 3. describes qualitatively the strength domain of the geomaterial in the $q - p'$ plane due
162 to chemical softening, i.e. for decreasing ζ. The scalars p' and q are respectively the Terzaghi
163 effective mean stress (i.e. the difference between the total mean stress and the pore pressure) and
164 the shearing stress intensity. The shearing stress intensity q is defined as the square root of the
165 second invariant of the deviatoric part, s_{ij}, of the stress tensor: $q = \sqrt{\frac{1}{2} s_{ij} s_{ji}}$. The Einstein
166 summation convention is adopted. In order to preserve the generality of the approach we consider
167 a general yield surface of the form:

$$f \equiv f\left(q, p', p'_c\right) = 0 \tag{1}$$

where p'_c is a material parameter (namely the yield stress under isotropic loading) which is assumed to decrease from p'_0 (initial reference state) to p'_R (residual yield stress once the chemical reaction is completed) according to the following law $p'_c \equiv p'_R - \left(p'_R - p'_0\right)\zeta^{\kappa}$ (Figure 3). κ is an exponent that can be experimentally determined for the material and the chemical process at hand.

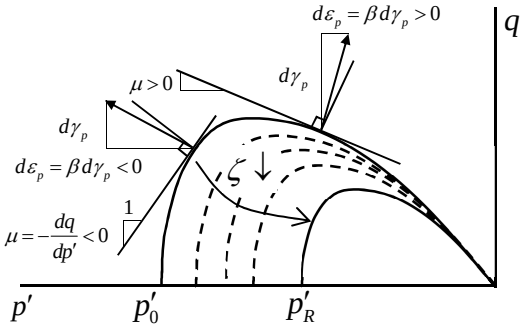

Figure 3. Chemical isotropic softening due to dissolution of a constituent. ζ describes the ratio of the residual mass of the constituent in the REV over its initial (reference) mass before the dissolution process. Compression is taken negative. $\beta>0$ corresponds to dilatancy and $\beta<0$ to contractancy (decrease of porosity).

In the frame of a small strain theory, the strain may be separated into elastic and plastic parts as follows:

$$\varepsilon = \varepsilon^e + \varepsilon^p \quad \text{and} \quad \gamma = \gamma^e + \gamma^p \tag{2}$$

where ε denotes the volumetric deformation and γ the shearing strain intensity $\gamma = \sqrt{2e_{ij}e_{ji}}$ with e_{ij} being the deviatoric strain tensor.

The elasto-plastic incremental stress-strain relationships are given by:

187 $$\dot{\boldsymbol{\sigma}}' = \mathbf{M}_{ep}\dot{\boldsymbol{\varepsilon}} + \boldsymbol{\Psi}\dot{\zeta} \tag{3}$$

188 where $\boldsymbol{\sigma}' = \begin{pmatrix} p' \\ q \end{pmatrix}$, $\boldsymbol{\varepsilon} = \begin{pmatrix} \varepsilon \\ \gamma \end{pmatrix}$, $\mathbf{M}_{ep} = \left[\mathbf{I} - \dfrac{\mathbf{M}_e \dfrac{\partial g}{\partial \boldsymbol{\sigma}} \left(\dfrac{\partial f}{\partial \boldsymbol{\sigma}} \right)^{\mathrm{T}}}{\left(\dfrac{\partial f}{\partial \boldsymbol{\sigma}} \right)^{\mathrm{T}} \mathbf{M}_e \dfrac{\partial g}{\partial \boldsymbol{\sigma}}} \right] \mathbf{M}_e$, $\boldsymbol{\Psi} = -\dfrac{\mathbf{M}_e \dfrac{\partial f}{\partial \zeta} \dfrac{\partial g}{\partial \boldsymbol{\sigma}}}{\left(\dfrac{\partial f}{\partial \boldsymbol{\sigma}} \right)^{\mathrm{T}} \mathbf{M}_e \dfrac{\partial g}{\partial \boldsymbol{\sigma}}}$, $\mathbf{I}$ is the identity

189 matrix and $\mathbf{M}_{\mathbf{e}} = \begin{pmatrix} K & 0 \\ 0 & G \end{pmatrix}$ the elasticity matrix. $(\bullet)^{\mathrm{T}}$ denotes the transpose of $(\bullet)$. K and G are

190 respectively the elastic bulk and the elastic shear moduli of the geomaterial. g is the plastic

191 potential which can be identified to the yield surface, f, in case of associate plasticity. For a

192 general plastic constitutive law, we can write:

193 $$\frac{\partial f}{\partial \boldsymbol{\sigma}} = \begin{pmatrix} \mu \\ 1 \end{pmatrix}, \quad \frac{\partial g}{\partial \boldsymbol{\sigma}} = \begin{pmatrix} \beta \\ 1 \end{pmatrix} \tag{4}$$

194 where β is the dilatancy angle ($\beta > 0$ for dilatant materials) and μ is the internal friction of the

195 geomaterial that depend on the actual state of stress. Using Eq.(4) we obtain:

196 $$\mathbf{M}_{ep} = \frac{GK}{G + \beta\mu K} \begin{pmatrix} 1 & -\beta \\ -\mu & \beta\mu \end{pmatrix} \tag{5}$$

197 and

198 $$\boldsymbol{\Psi} = \frac{1}{G + \beta\mu K} \begin{pmatrix} \beta K \\ G \end{pmatrix} \frac{\partial f}{\partial \zeta} \tag{6}$$

199 with

200 $$\frac{\partial f}{\partial \zeta} = \frac{\partial f}{\partial p'_c} \frac{dp'_c}{d\zeta} = \frac{\partial f}{\partial p'_c} \kappa \left(p'_R - p'_0 \right) \zeta^{\kappa - 1} \tag{7}$$

201 It is worth mentioning, that under constant loading, chemical softening would result in the

202 gradual accumulation of plastic deformations, which are controlled by the dissolution reaction

203 kinetics. This accumulation of deformations under constant loading can be seen as a creep

behavior induced by the chemical process of dissolution. Creep phenomena due to reactive fluids injection are observed in laboratory tests on porous rocks [*Le Guen et al.*, 2007; *Liteanu and Spiers*, 2009; *Shin and Santamarina*, 2009; *Brantut et al.*, 2013; *Croizet et al.*, 2013].

2.2. Mass balance

The dissolution of minerals is described by appropriate chemical reactions. According to the reaction's stoichiometry the minerals of a rock may be degraded and transformed to amorphous solid or liquid. For example the dissolution/precipitation of quartz in water is described by the following chemical equation:

(R1) $$SiO_2(\text{solid}) + 2H_2O(\text{liquid}) \rightleftharpoons H_4SiO_4(\text{aqueous solution})$$

At equilibrium the silicic acid (H_4SiO_4) is dissolved in the water with a concentration of the order of few ppm. Another example is the dissolution of calcite with water that is saturated with carbon dioxide:

(R2) $$CaCO_3(\text{solid}) + H_2CO_3(\text{aqueous solution}) \rightleftharpoons Ca(HCO_3)_2(\text{aqueous solution})$$

This equation represents a set of consecutive reactions that take place and are responsible for the dissolution of carbonate rocks [*Grgic*, 2011].

Here we consider any dissolution process of the form:

(R3) $$\underset{(3)}{\text{solid}} + \underset{(1)}{\text{solvent}} \rightleftharpoons \underset{(2)}{\text{solution}}$$

The reaction kinetics of this general equation will be analyzed in the next section.

At the macro-scale, the REV can be seen as a porous medium. The mass of the solid phase is M_3 (e.g. SiO_2) and the mass of the fluid phase is $M_f = M_1 + M_2$, where M_1 is the mass of the solvent (e.g. H_2O) and M_2 the mass of the dissolution product (e.g. H_4SiO_4).

Following the notation of Coussy [2004] the mass balance equations hold:

$$\frac{d^{f}M_1}{dt}=\frac{d}{dt}\left(\rho_{f1}n_1 d\Omega_t\right)=\mathring{r}_{1\to 2}\,d\Omega_t \tag{8}$$

$$\frac{d^{f}M_2}{dt}=\frac{d}{dt}\left(\rho_{f2}n_2 d\Omega_t\right)=\left(\mathring{r}_{2\to 1}+\mathring{r}_{2\to 3}\right)d\Omega_t \tag{9}$$

$$\frac{d^{s}M_3}{dt}=\frac{d}{dt}\left[\rho_s\left(1-n\right)d\Omega_t\right]=\mathring{r}_{3\to 2}\,d\Omega_t \tag{10}$$

where $\frac{d^{\chi}}{dt}$ is the particle derivative, ρ_χ is the density and n_χ is the Eulerian porosity referring to particle χ (f for fluid and s for solid species), $\mathring{r}_{\chi\to\psi}$ represents the rate of mass of χ transformed to ψ and $d\Omega_t$ is the material volume in the current configuration. By definition:

$$\rho_{f1}n_1+\rho_{f2}n_2=\rho_f n \tag{11}$$

where ρ_f is the density of the solution, which depends on the reactant's concentrations, the pressure p_f and the temperature. Equations (8) and (9) lead to:

$$\frac{d^{f}}{dt}\left(\rho_f n d\Omega_t\right)=\mathring{r}_{2\to 3}\,d\Omega_t \tag{12}$$

Considering isothermal conditions and constant density for the solid phase, Eqs.(10) and (12) become:

$$-\frac{\partial n}{\partial t}+\nabla_{\mathbf{X}}\mathbf{V}_s-\nabla_{\mathbf{X}}\left(n\mathbf{V}_s\right)=-\frac{1}{\rho_s}\mathring{r}_{2\to 3} \tag{13}$$

$$\frac{\partial n}{\partial t}+n\frac{1}{\rho_f}\frac{\partial\rho_f}{\partial p_f}\frac{\partial p_f}{\partial t}+n\frac{1}{\rho_f}\frac{\partial\rho_f}{\partial w_2}\frac{\partial w_2^M}{\partial t}+\frac{1}{\rho_f}\nabla_{\mathbf{X}}\left(\rho_f\right)n\mathbf{V}_f+\nabla_{\mathbf{X}}\left(n\mathbf{V}_f\right)=\frac{1}{\rho_f}\mathring{r}_{2\to 3} \tag{14}$$

where the Nabla operator refers to the initial configuration ($\mathbf{X}$ is the position vector of the solid particles in the initial configuration), $\mathbf{V}_s$ and $\mathbf{V}_f$ are respectively the velocities of the solid phase

and fluid particles, p_f the fluid pressure and $w_2^M = \frac{M_2}{M_f}$ the average dissolution product to fluid mass fraction over the REV (macro-scale). Adding Eqs. (13) and (14) and using the chain rule, the pore pressure diffusion-generation equation is obtained:

$$\frac{\partial p_f}{\partial t} = c_{hy}\nabla_{\mathbf{x}}^2 p_f - \frac{1}{\beta^*}\frac{\partial \varepsilon}{\partial t} - c_{p,ch}\frac{\partial w_2}{\partial t} \tag{15}$$

where c_{hy} is the hydraulic diffusivity and $\beta^* = n\beta_f$ with $\beta_f = \frac{1}{\rho_f}\frac{\partial \rho_f}{\partial p_f}$ is the compressibility of the fluid [see also *Ghabezloo and Sulem*, 2008]. For plastic incompressibility of the solid phase and of the fluid, $\beta^* = \frac{1}{K}$. For the derivation of the pore pressure diffusion-generation equation, the Darcy law was assumed and the gradient of the density of the fluid was ignored as being negligible compared to the other terms of the equation. The deformation of the solid skeleton, i.e. the term $\nabla_{\mathbf{x}}\mathbf{V}_s = \frac{\partial \varepsilon}{\partial t}$, is responsible for the hydro-mechanical coupling. In the right hand side of the equation the last term expresses the pore pressure change due to dissolution/precipitation process and $c_{p,ch}$ is the chemical pressurization coefficient, which depends on the evolution of the fluid density because of the reaction process. Herein, we neglect this effect as it does not affect the stability of the system and generally its influence is limited [*Stefanou and Sulem*, 2013]. Finally, for small strains $\nabla_{\mathbf{X}} \approx \nabla_{\mathbf{x}}$, where $\mathbf{x}$ is the position vector of the solid particles in the current configuration.

2.3. Momentum balance under oedometric conditions

Under oedometric conditions the stress equilibrium is expressed as follows:

$$\sigma_{zz,z} = 0 \tag{16}$$

where $\sigma_{ij} = \sigma'_{ij} - p_f\delta_{ij}$, δ_{ij} is the Kronecker delta, $\sigma_{zz} = p - \frac{2}{\sqrt{3}}q$, $\gamma = -\frac{2}{\sqrt{3}}\varepsilon_{zz}$, $\varepsilon = \varepsilon_{zz}$, $\varepsilon_{zz} = u_{z,z}$ $\varepsilon_{rr} = \varepsilon_{\theta\theta} = 0$ (for axisymmetric conditions). Using Eq.(3) we obtain:

$$\dot{\sigma}'_{zz} = c\left(\Lambda \dot{\varepsilon}_{zz} + \frac{\partial f}{\partial \zeta}\dot{\zeta}\right) \tag{17}$$

where $\Lambda = K\dfrac{\left(1+\frac{2}{\sqrt{3}}\beta\right)\left(1+\frac{2}{\sqrt{3}}\mu\right)}{\frac{2}{\sqrt{3}}-\beta\frac{K}{G}}$ and $c = \dfrac{\frac{2}{\sqrt{3}}-\beta\frac{K}{G}}{1+\beta\mu\frac{K}{G}}$. $c\Lambda$ expresses the change of the effective vertical stress due to compaction and $c\dfrac{\partial f}{\partial \zeta}$ its change due to chemical degradation.

3. Micro-scale

3.1. Cataclasis, solid skeleton damage and evolution of the effective grain size

A rock can be seen as an assemblage of bonded grains, which during deformation may break into smaller grains with rupture of bonds. Following Lade et al. [1996] the grain size reduction is related to the total energy input. In this sense, at least part of the mechanical energy is dissipated through various micro-mechanisms for the creation of new surfaces in the medium (grain fracturing). “Hertzian cracks” at the grain contacts (intergranular fracturing, grain crushing, grain attrition etc.), “microcracking” of the cementitious matrix [*Aydin and Ahmadov*, 2009; *Cilona et al.*, 2012] and grain debonding [*Castellanza and Nova*, 2004] are some important mechanisms that lead to the reduction of the effective grain size of the geomaterial and consequently to the increase of the dissolution front.

Under this framework, it is convenient to define an effective grain size, D, whose evolution reflects the effect of grain damage. According to Lade et al. [1996], for a given grain size distribution, this effective grain size is commonly taken equal to D_{10} (10% of the system weight consists of grains below D_{10} diameter). Generally, the choice of the appropriate effective grain size depends on the exact grain size distribution and the material at hand. For instance in the case of shear bands created in the laboratory D_{10} seems a good measure for the effective grain size reduction [*El Bied et al.*, 2002]. On the other hand, in the case of compaction bands observed in the field, D_{50} seems a better choice [*Cilona et al.*, 2012].

Lade et al. [1996] proposed the following expression for the evolution of grain crushing of a granular material in terms of the mechanical work input:

$$D = D_0 \left(\frac{a}{a + E_T} \right) \tag{18}$$

where D_0 is the effective grain size of the initial gradation and E_T is the total energy input per specimen unit volume (including the energy due to isotropic compression and shearing). a is a fitting parameter, which will be called here grain damage sensitivity parameter that expresses the extent of the grain size change due to energy input. For large values of parameter *a*, as compared to E_T, the grain size is constant. As discussed by Lade et al. [1996], the total energy seems to be a more relevant parameter for describing grain breakage compared to the effective mean stress or the void ratio. As an example, for Cambria sand $a = 0.747\text{MPa}$ [*Lade et al.*, 1996]. For a rock, the parameter a should also depend on the grain size distribution [cf. *Cheung et al.*, 2012]. Considering that the specific effective surface of a grain S (effective grain surface area to volume ratio) is inversely proportional to the grain diameter, it is natural to assume the same type of relationship:

$$S = S_0 \left(1 + \frac{E_T}{a} \right) \tag{19}$$

It is worth emphasizing that the grains of rocks are often cemented together and that the consideration of the rock as a granular material, with well-defined grain to pore fluid interactions is rather an idealization of reality. Nevertheless, as it was mentioned above, the dissipation during mechanical loading is mainly attributed to internal friction mechanisms (reorganization of grains, grain dislocation/disclination) and microcracking of both the grains and of the cementitious matrix (Hertzian cracking, microcracking, debonding etc.). In this sense, Eq.(19), could also be used in order to describe the increase of the specific surface of the grains of a cemented granular material like a porous rock. Parameter a may be calibrated either through appropriate micromechanical models that take into account the micro-cracking of the matrix and grain breakage [e.g. *Das et al.*, 2011] or through adequate experimental tests. More specifically, the value of the grain damage parameter may be determined experimentally through acoustic

316 emissions, X-ray tomography or other experimental techniques [*Wong and Baud*, 2012] that will
317 correlate the effective grain size due to grain damage and the mechanical energy input.
318
319 Finally, it should be mentioned that grain crushing results in a reduction of porosity and generally
320 to a reduction of permeability [*Walsh and Brace*, 1984; *Sulem and Ouffroukh*, 2006]. Moreover,
321 due to dissolution, the specific area of the grains at the microscale is increased and the existing
322 microcracks propagate further (subcritical growth, stress corrosion cracking). Therefore, the grain
323 crushing sensitivity parameter, a, is not necessarily constant in time and may depend on the
324 reaction kinetics, the stress level and the nature of the saturating fluid. However, in the linear
325 stability analysis presented in the next section, the permeability change due to porosity reduction
326 is of second order and can be neglected for the onset of strain localization. Nevertheless, for
327 performing numerical simulations of rocks with the proposed chemo-poro-mechanical model it is
328 possible to determine the evolution of these parameters based on empirical and/or theoretical
329 models.
330
331 ***3.2. Reaction kinetics***
332 According to Rimstidt and Barnes [1980] the rate of reaction between the fluid and solid phase
333 during quartz dissolution (or precipitation, R1) is directly proportional to the interfacial area
334 between the solid and the liquid phase. The dissolution rate is commonly assumed to be
335 proportional to the mineral surface area exposed to the aqueous solution [*Cubillas et al.*, 2005].
336 Here we generalize this idea for any dissolution process of the form of R3. The rate of production
337 (or consumption) of moles of the dissolution product is considered to obey the following rate
338 equation:

339 $$\frac{\partial n_2}{\partial t} = Ak\left(1-\Omega\right) \tag{20}$$

340 where n_2 is the number of moles of the product of the dissolution process (e.g. the H_4SiO_4 or the
341 $Ca\left(HCO_3\right)_2$), A the available interfacial area of the solid with the solution, k the dissolution
342 rate constant per unit area of the interface and Ω is the degree of saturation. If $\Omega = 1$ the reaction

is at equilibrium, if $\Omega < 1$ dissolution takes place and if $\Omega > 1$ precipitation happens. Ω is expressed in terms of the reaction quotient, Q, and the equilibrium constant, K_{eq}, as follows:

$$\Omega = \frac{Q}{K_{eq}} \tag{21}$$

It is worth mentioning that in order to account for the intergranular dissolution-diffusion micro-mechanisms that take place in the thin aqueous film that is developed at the grain contacts, a chemical potential that depends on the stress state is often considered (pressure solution [*Rutter*, 1983]). As a result, the reaction kinetics (i.e. Eq. (20), equilibrium constant, reaction rate) might be functions of the stress state. However, intense cataclasis (stress induced cracking, grain breakage, microcracking, debonding etc.) is often observed inside the zone of deformation bands [*Baud et al.*, 2009; *Cilona et al.*, 2012]. Therefore, in the stability analysis performed in the next section, the reaction kinetics will not directly depend on the stress state, but will be a function of the available interaction surface of the reactants (dissolution of grains), which depends on the stress state because of grain damage.

Assuming that the reaction activity coefficients for the reactants are close to unity and that $w_2 \ll 1$, Eq.(20) and (21) give (Appendix A.1):

$$\frac{\partial w_2}{\partial t} = k^* \frac{S}{e}\left(1 - \frac{w_2}{w_2^{eq}}\right) \tag{22}$$

where $k^* = \frac{\mu_2}{\rho_f} k$, $e = \frac{n}{1-n}$ is the void ratio and w_2^{eq} the mass fraction of dissolution product to the fluid mass at chemical equilibrium. It should be emphasized that Eq.(22) is written at the microscale and that w_2, S and e represent local quantities, which are not necessarily homogeneous over the REV (Figure 2). On the other hand, the constitutive law and the mass balance represent quantities defined over the REV and therefore the aforementioned local quantities have to be upscaled from the micro- to the macro-level.

3.3. Chemical softening and upscaling

At the macroscale the rate of the chemical softening parameter ζ holds for $w_2 \ll 1$ (Appendix A.2):

$$\frac{\partial \zeta}{\partial t} = -\frac{\mu_3}{\mu_2}\frac{\rho_f}{\rho_s} e \zeta \frac{\partial w_2^M}{\partial t} \tag{23}$$

The average mass fraction of the dissolution product over the REV (macro-level) is related to the local mass fraction w_2 (Figure 2) as follows:

$$w_2^M = \frac{1}{V_T}\int_{V_T} w_2 dV \tag{24}$$

Assuming that $w_2 = w_2(z,t)$ (oedometric conditions) is a function that can be expanded into Taylor series up to the second order in z:

$$w_2(z_l,t) \approx w_2(z,t) + z_l \left.\frac{\partial w_2(z,t)}{\partial z}\right|_z + \frac{1}{2} z_l^2 \left.\frac{\partial^2 w_2(z,t)}{\partial z^2}\right|_z \tag{25}$$

where z_l is the coordinate in a local coordinate system with origins at the center of the REV, z, injecting equation (25) to equation (24) and integrating over the REV we obtain:

$$w_2^M \approx w_2 + \ell_c^2 \frac{\partial^2 w_2}{\partial z^2} \tag{26}$$

where $\ell_c = \ell_{REV}\sqrt{\frac{1}{24}} \simeq \frac{\ell_{REV}}{5}$ appears as a characteristic internal length and ℓ_{REV} is the size of the REV in the z direction. Note that if the mass fraction is homogeneous all over the REV, then $w_2^M = w_2$.

4. Compaction band formation

Equations (15), (16) and (22) describe the evolution of the system under oedometric conditions, while equation (26) links the macro- and micro-scale. Introducing the dimensionless quantities:

386
$$\hat{w}_2^{(M)} = \frac{w_2^{(M)}}{K_{eq}}, \quad \hat{p}_f = \frac{p_f}{\sigma_n}, \quad \hat{\sigma}_{ij} = \frac{\sigma_{ij}}{\sigma_n}, \quad \hat{p} = \frac{p}{\sigma_n}, \quad \hat{q} = \frac{q}{\sigma_n}, \quad \hat{E}_T = \frac{E_T}{\sigma_n}, \quad \hat{a} = \frac{a}{\sigma_n}, \quad \hat{\beta}^* = \beta^* \sigma_n$$
$$\hat{u}_i = \frac{u_i}{D_0^{50}}, \quad \hat{L} = \frac{L}{D_0^{50}}, \quad \hat{S} = S\, D_0^{50}, \quad \hat{\rho}_\chi = \frac{\rho_\chi}{\rho_{H_2O}}, \quad \hat{t} = \frac{t}{T}, \quad \hat{c}_{hy} = \frac{T}{\left(D_0^{50}\right)^2} c_{hy}$$

387 (27)

388 with D_0^{50} the median grain diameter in the reference/initial state and choosing $T = \frac{K_2^{eq} D_0^{50}}{k^*}$ as
389 characteristic time, the aforementioned equations become:

390
$$\hat{\sigma}_{zz,\hat{z}} = 0 \tag{28}$$

391
$$\frac{\partial \hat{p}_f}{\partial \hat{t}} = \hat{c}_{hy} \frac{\partial^2 \hat{p}_f}{\partial \hat{z}^2} - \frac{1}{\hat{\beta}^*} \frac{\partial \varepsilon}{\partial \hat{t}} - \hat{c}_{p,ch} \frac{\partial \hat{w}_2^M}{\partial \hat{t}} \tag{29}$$

392
$$\frac{\partial \hat{w}_2}{\partial \hat{t}} = e^{-1} \hat{S} \left(1 - \hat{w}_2\right) \tag{30}$$

393
$$\hat{w}_2^M \approx \hat{w}_2 + \hat{\ell}_c^2 \frac{\partial^2 \hat{w}_2}{\partial \hat{z}^2} \tag{31}$$

394 In the following the hats over the variables will be dropped in order to simplify the notations.
395
396 It has to be mentioned that the application of the well-known localization (bifurcation) criterion
397 of Issen & Rudnicki [*Rudnicki and Rice*, 1975; see also *Rice*, 1976; *Bigoni and Hueckel*, 1991;
398 *Issen and Rudnicki*, 2000] is not straightforward in the present case where a chemo-poro-
399 mechanical coupling takes place. For this reason a linear stability analysis is performed in the
400 next section.
401
402 ***4.1. Linear stability analysis***
403 Let u_z^h, p_f^h and w_2^h be the solutions of the above equations that lead to homogeneous
404 deformation in space and $\tilde{u}_z(z,t)$, $\tilde{p}_f(z,t)$ and $\tilde{w}_2(z,t)$ perturbations such that:

$$\begin{aligned} u_z(z,t) &= u_z^h + \tilde{u}_z(z,t) \\ p_f(z,t) &= p_f^h + \tilde{p}_f(z,t) \\ w_2(z,t) &= w_2^h + \tilde{w}_2(z,t) \end{aligned} \tag{32}$$

The spatial dependence of the perturbations is decomposed into Fourier modes with wavelength λ. Assuming zero fluid flux and no reaction evolution at the boundaries of the model:

$$\tilde{u}_z(z,t) = Ue^{st}\sin\left(\frac{z}{\ell}\right),\ \tilde{p}_f(z,t) = Pe^{st}\cos\left(\frac{z}{\ell}\right) \text{ and } \tilde{w}_2(z,t) = We^{st}\cos\left(\frac{z}{\ell}\right) \tag{33}$$

where $\lambda = 2\pi\ell = L/N$, N is equal to an integer satisfying the zero fluid flux and reaction evolution at the boundary $z = \pm L/2$, and s is the growth coefficient of the perturbation (Lyapunov exponent). $s > 0$ means local instability.

Introducing the above perturbations to Eqs.(28)-(30) and neglecting the higher order terms we obtain the system:

$$\tilde{\sigma}_{zz,z} = 0 \tag{34}$$

$$\frac{\partial \tilde{p}_f}{\partial t} = c_{hy}\frac{\partial^2 \tilde{p}_f}{\partial z^2} - \frac{1}{\beta^*}\frac{\partial \tilde{\varepsilon}}{\partial t} \tag{35}$$

$$\frac{\partial \tilde{w}_2}{\partial t} = \frac{1-w_2^h}{e^h}\tilde{S} - \frac{S^h}{e^h}\left[1+\eta^h\left(1-w_2^h\right)\right]\tilde{w}_2 \tag{36}$$

$$\tilde{w}_2^M \approx \tilde{w}_2 + \ell_c^2\frac{\partial^2 \tilde{w}_2}{\partial z^2} \tag{37}$$

where $\eta^h = \frac{\mu_3}{\mu_2}\left(1+e^h\frac{\rho_f}{\rho_s}\right)$. The superscript '*h*' denotes the homogeneous state of the system. $\tilde{S}$ represents the perturbation of the specific surface because of the perturbations introduced in Eq.(32) and because of Eq.(19). All the above quantities are dimensionless (the hats were dropped for simplicity).

423

424 Substituting Eqs.(33) in the above equations, we obtain the following system of equations in
425 matrix form:

426 $$\mathbf{A}\cdot\mathbf{X}=\mathbf{0} \tag{38}$$

427 where $\mathbf{A}=\begin{pmatrix} \frac{A_{11}}{\ell^2} & -\frac{1}{\ell} & \frac{A_{13}}{\ell}\left(1-\frac{\ell_c^2}{\ell^2}\right) \\ -\frac{\mathrm{s}}{\ell}\frac{1}{\beta^*} & s+\frac{c_{hy}}{\ell^2} & 0 \\ -\frac{A_{32}S^h}{\ell} & 0 & \mathrm{s}+S^h\varphi \end{pmatrix}$,

428 $A_{11}=-K\dfrac{\left(\frac{2\beta}{\sqrt{3}}+1\right)\left(\frac{2\mu}{\sqrt{3}}+1\right)}{1+\frac{K}{G}\beta\mu}$, $A_{13}=-\dfrac{\left(\frac{2}{\sqrt{3}}-\frac{K}{G}\beta\right)}{1+\frac{K}{G}\beta\mu}\dfrac{\partial f}{\partial\zeta}\zeta^h e^h\dfrac{\rho_f\mu_3}{\rho_s\mu_2}$, $A_{32}=\dfrac{1-w^h}{ae^h}$,

429 $\varphi=\dfrac{1}{e^h}\left[1+\eta^h\left(1-w^h\right)\right]$ and $\mathbf{X}=\begin{pmatrix} U \\ P \\ W \end{pmatrix}$.

430

431 The system has non trivial solutions when the determinant of $\mathbf{A}$ is zero, i.e. $Det[\mathbf{A}]=0$, or
432 equivalently:

433 $$s^2+C_1 s+C_0=0 \tag{39}$$

434 with $C_0=\dfrac{S^h\beta^* c_{hy}}{\ell^2}\dfrac{\varphi A_{11}+A_{13}A_{32}\left(1-\frac{\ell_c^2}{\ell^2}\right)}{A_{11}\beta^*-1}$ and

435 $C_1=S^h\varphi+\dfrac{A_{11}c_{hy}}{A_{11}\beta^*-1}\dfrac{1}{\ell^2}+S^h\dfrac{A_{13}A_{32}}{A_{11}\beta^*-1}\left(1-\dfrac{\ell_c^2}{\ell^2}\right)$.

436

437 If the real part of a root of the above quadratic equation (characteristic polynomial) is positive
438 then the system is unstable.

439

440 ***4.2. Conditions for instability***

441 The roots s_1 and s_2 of the above quadratic equation satisfy:

442 $$s_1 s_2 = C_0 \text{ and } s_1 + s_2 = -C_1 \tag{40}$$

443 Therefore if $C_0 < 0$ then at least one root with positive real part exists. For $A_{11} < 0$ and $w^s < 1$

444 (start of the reaction), $C_0 < 0$ gives:

445 $$\varphi A_{11} + A_{13} A_{32} \left(1 - \frac{\ell_c^2}{\ell^2} \right) > 0 \tag{41}$$

446 or

447 $$\frac{\partial f}{\partial \zeta} \zeta^h \left(1 - \frac{\ell_c^2}{\ell^2} \right) < C_{cr} \tag{42}$$

448 where $C_{cr} = -\frac{\Lambda}{\Xi} \frac{\rho_s \mu_2}{\rho_f \mu_3}$ and $\Xi = \frac{1 - w^h}{\varphi a}$. This expression accounts for chemical softening due to

449 dissolution and includes the characteristic length of the REV. When dissolution occurs, $w^h < 1$

450 and $\Xi > 0$. Moreover, in compression, $d\varepsilon_{zz}^p = d\varepsilon^p < 0$ and therefore $\beta < 0$. Consequently, Λ is

451 positive and C_{cr} is negative. Λ expresses the increase of the effective compressive stress

452 because of compaction (see Eq.(17)). $\frac{\partial f(\zeta)}{\partial \zeta} < 0$ expresses the contraction of the elastic domain

453 (chemical softening) because of dissolution. Ξ represents the effect of dissolution on the stability

454 of the system due to grain damage. The bigger the value of Ξ is (i.e., high effect of dissolution

455 due to grain damage) the more unstable the system becomes, as the instability condition (42) is

456 satisfied for a larger spectrum of μ and β values (the instability region in the $q - p$ plane is

457 larger). The role of Ξ will be explored in the next paragraph

458 In the special case where $C_{cr} = 0$ ($\mu = -\frac{\sqrt{3}}{2}$ or $\beta = -\frac{\sqrt{3}}{2}$ leading to $\Lambda = 0$), Eq. (42) becomes:

$$\frac{\partial f}{\partial \zeta}\left(1-\frac{\ell_c^2}{\ell^2}\right)<0 \tag{43}$$

and the system is unstable if $\ell > \ell_c$. In other words, the instability travels in space with a finite wavelength ($\lambda > 2\pi\ell_c \simeq 1.2\ell_{REV}$) resulting in a compaction band of finite thickness. This will be further investigated in the next paragraphs. Notice that in the absence of mechanical softening and internal length ($\ell_c = 0$) the above condition for compaction band instabilities ($\mu = -\frac{\sqrt{3}}{2}$ or $\beta = -\frac{\sqrt{3}}{2}$) coincides with the condition derived by Issen & Rudnicki [2000].

Finally, the above sufficient condition for instability should be completed with the following condition in order to avoid the consideration of flutter instabilities, which are characterized by the fact that the roots of the characteristic polynomial have an imaginary part:

$$C_1^2 - 4C_0 \geq 0 \tag{44}$$

The reason for excluding this kind of oscillatory instabilities (blowing-up oscillations) is that they seem unphysical for the chemo-mechanical problem at hand.

4.3. Regions of stability and parameters sensitivity

As an example of a cap yield surface we consider a modified Cam-clay yield surface with an associate flow rule. Certainly, modified Cam-clay with associate flow rule is not the best constitutive model for rocks and in order to obtain quantitative results an extensive experimental research has to be conducted. Nevertheless, it is expected, that a general cap model, (Figure 3) will be overall appropriate [*Baud et al.*, 2006; *Wong and Baud*, 2012]. Herein, we choose the modified Cam-clay plasticity model with associate flow rule due to its relatively simple form (i.e. elliptic yield cap). In particular the adopted yield surface is (Figure 4):

$$f \equiv q^2 + M^2 p'(p' - p'_c) = 0 \tag{45}$$

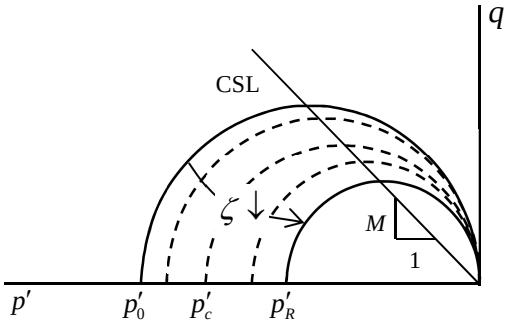

Figure 4. Modified Cam-clay model with chemical softening. Compression negative. CSL stands for the critical state line, which is assumed constant.

In this way the qualitative behavior of the system may be studied pointing out the effects of chemical softening to compaction band formation. For the example at hand we consider the following dimensionless parameters: $p'_0 = -1$, $p'_R = -0.2$, $p_f = 0.4$, $M = 1$, $\kappa = 1$, $K = G = 100$, $S = 1$, $c_{hy} = 6 \times 10^7$, $\frac{\mu_3}{\mu_2} = 0.6$, $\frac{\rho_f}{\rho_s} = 0.4$. In this paragraph we assume that $\ell_c = 0$, or in other words we consider that the rock microstructure is homogeneous (see section 3.3). This assumption does not influence the conditions for the onset of the compaction band formation (see Eqs. (42) or (43)), which is the purpose of the current paragraph. In the next paragraph the heterogeneity of the REV will be considered and its influence to compaction bands thickness/periodicity will be explored.

According to Eq.(42) compaction band triggering depends on Ξ, which represents the tendency of the system for compaction band formation. With higher values of Ξ, the region of instability in $q - p$ plane becomes larger. Figure 5 and Figure 6 show the dependency of Ξ on the grain fracturing coefficient a for $n = 0.25$ and on the porosity n for $a = 0.1$ respectively. Notice that when the solution is saturated, $w_2^h = 1$ (i.e. the dissolution process stops), compaction bands can be triggered only if $\beta = -\frac{\sqrt{3}}{2}$ or $\mu = -\frac{\sqrt{3}}{2}$. This is consistent with the Issen and Rudnicki condition for compaction bands [*Issen and Rudnicki,* 2000]. The same holds when no grain damage occurs ($a \to \infty$) or when the medium is not porous ($n \to 0$), as no reaction takes place

and chemical softening is impossible. According to Figure 6, in the case of layered materials, compaction bands would preferentially develop in the more porous layers.

Figure 7, Figure 8 and Figure 9 show the region of instability in the $q-p$ plane for various values of the grain damage coefficient, a, for $w_2^h = 0$ and for $n = 0.25$. If at a certain time the stress state in the *q-p* plane is inside this instability region then compaction bands instabilities are triggered. Notice that because of the strong chemo-mechanical coupling of the proposed model, the instability manifold is larger than the instability manifold defined by the Issen & Rudnicki [2000] compaction band criterion (see Figure 7 to Figure 9) and its size depends on the grain damage parameter a. Moreover, compaction bands can be triggered even for $\beta + \mu > -\sqrt{3}$. Figure 10 shows the growth coefficient *s* as a function of the wavelength of the perturbation for $a = 10^{-2}$, $w_2^h = 0$, $n = 0.25$, $p = 1.2$, $q = 0.4$ and $\zeta = 1$. s is positive and the system is unstable.

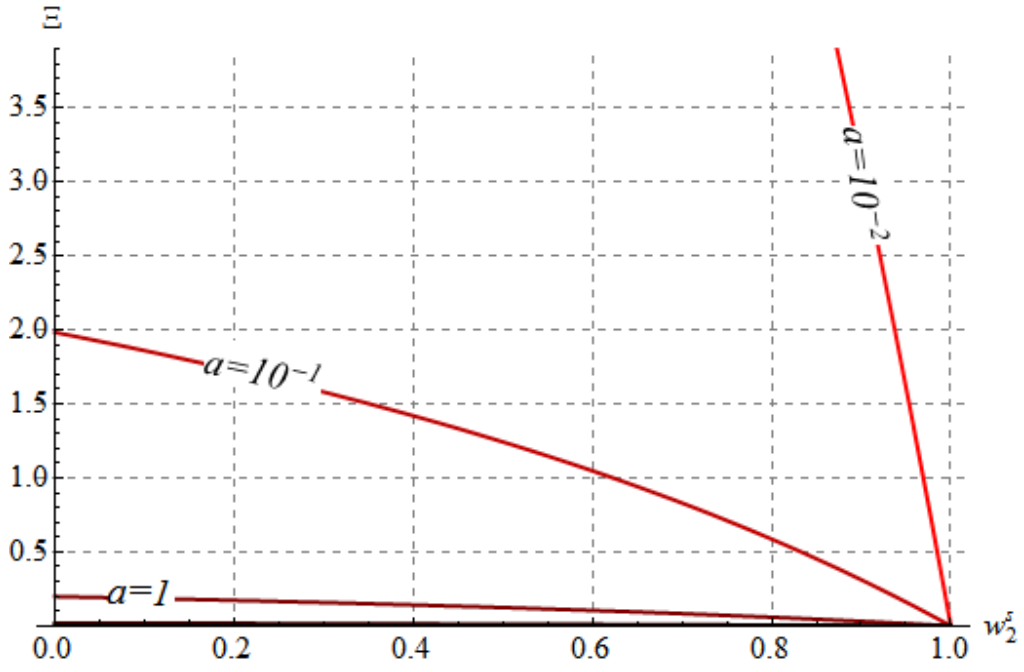

Figure 5. Tendency for compaction bands for $n = 0.25$. The more crushable the grains are, i.e. a small, the bigger the coefficient Ξ and the larger the region of instability is in $q-p$ plane.

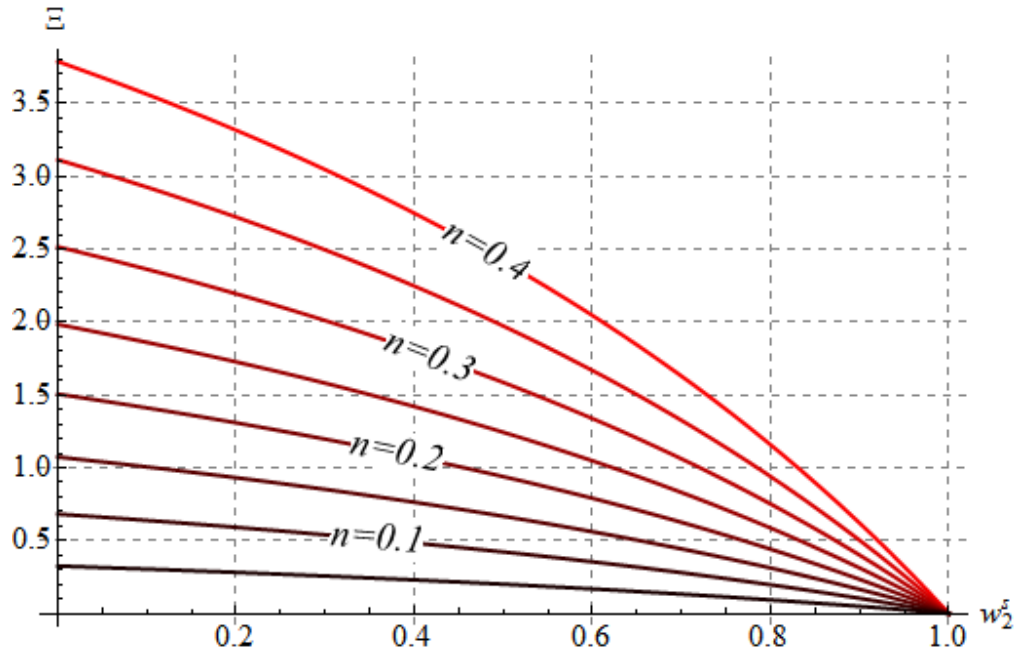

519

520 *Figure 6. Tendency for compaction bands for* $a = 0.1$. *The more porous the geomaterial is, the*
521 *bigger the coefficient* Ξ *and the larger the region of instability in* $q - p$ *plane are.*

522

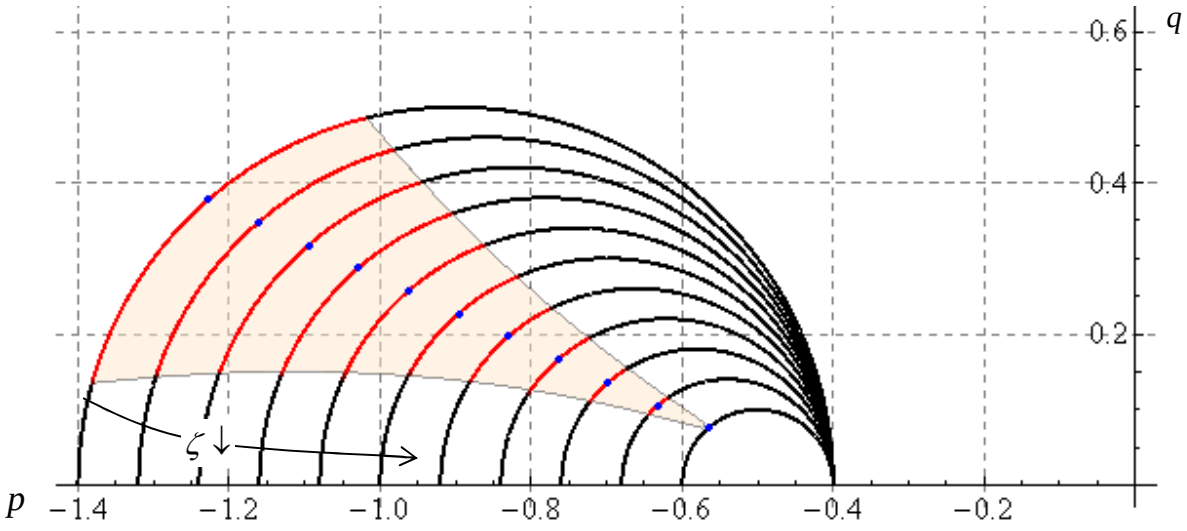

523

524 *Figure 7. Instability region (shaded) for compaction bands under oedometric conditions for*
525 $a = 10^{-3}$ *(*$\Xi = 200$*). The points (in blue) represent the Issen & Rudnicki criterion for compaction*
526 *band instabilities. Different yield surfaces are drawn for different levels of chemical degradation*
527 ζ .

528

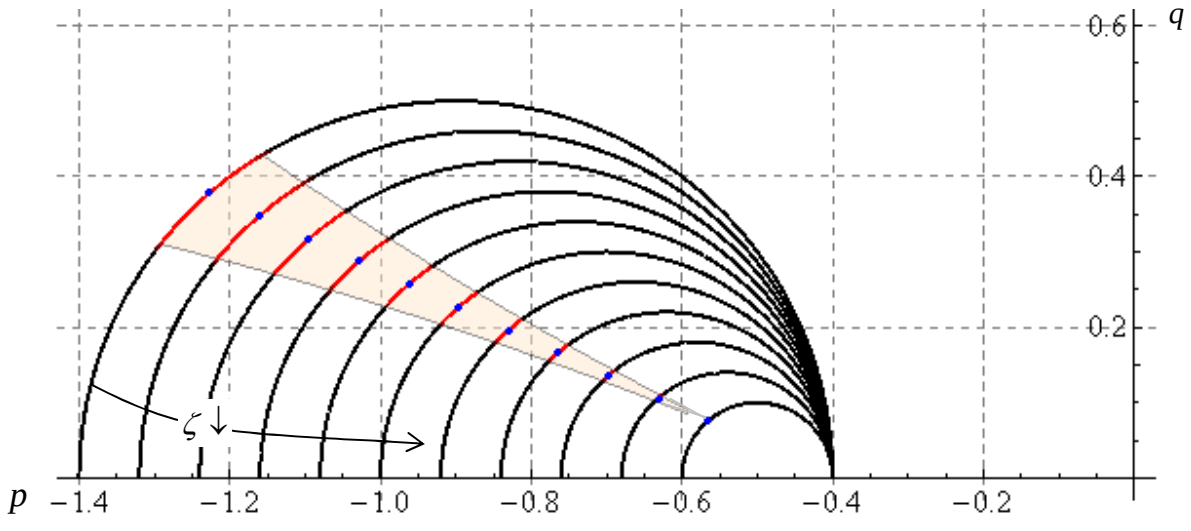

Figure 8. Instability region (shaded) for compaction bands under oedometric conditions for $a = 10^{-2}$ *(*$\Xi = 20$*). The points (in blue) represent the Issen & Rudnincky criterion for compaction band instabilities. Different yield surfaces are drawn for different levels of chemical degradation* ζ *.*

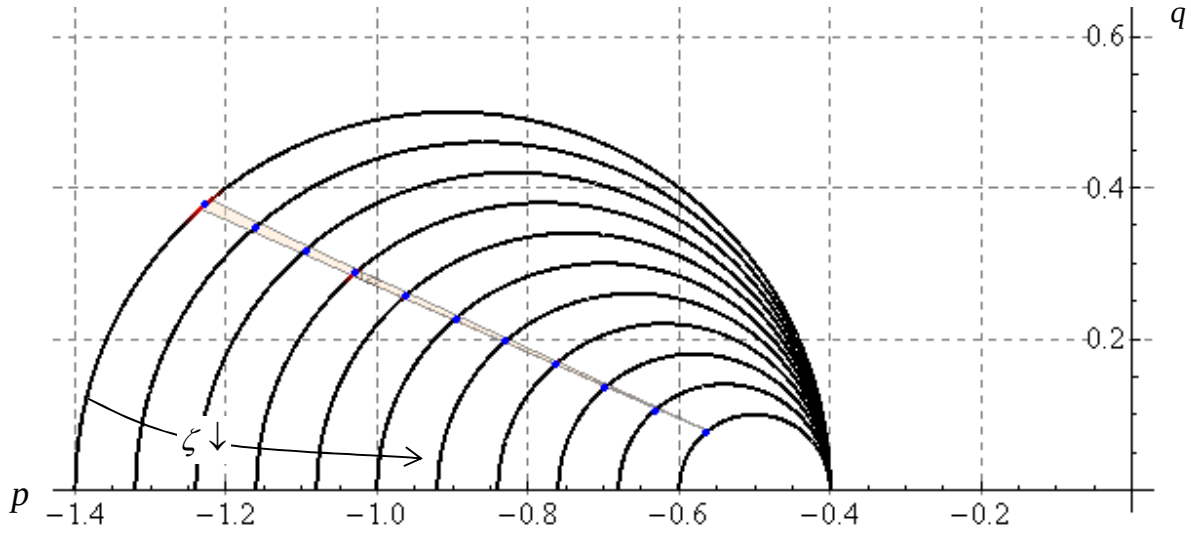

Figure 9. Instability region (shaded) for compaction bands under oedometric conditions for $a = 1$ *(*$\Xi = 2$*). The points (in blue) represent the Issen & Rudnincky criterion for compaction bands. Different yield surfaces are drawn for different levels of chemical degradation* ζ *.*

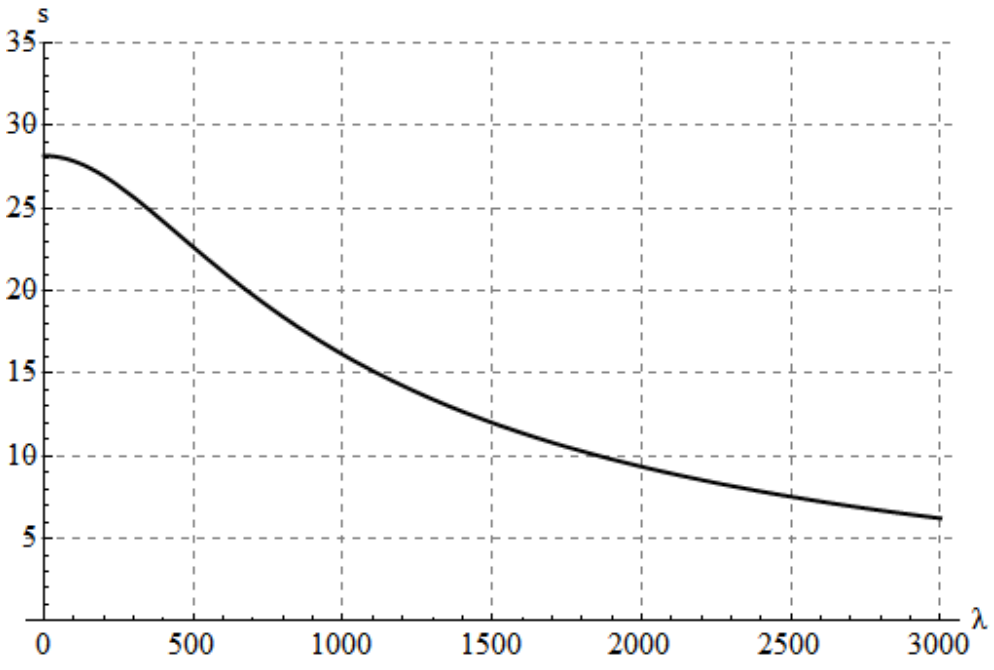

Figure 10. Instability growth coefficient s in terms of the perturbation wavelength λ for $\ell_c = 0$. The growth coefficient is positive and the system is unstable.

4.4. Wave length selection

Figure 10 shows that the perturbation that travels fastest (maximum growth coefficient - dominant wave length) has zero wavelength. In other words, the dominant wavelength, $\lambda_{\max}$, is zero. This means that the deformation would be localized in a zone of an infinitesimal thickness as time increases (see Eq.(33)) or equivalently that the compaction bands would be infinitesimally close to each other ($spacing = \lambda_{\max} = L_b / N = 0$ and so for given $L = L_b$ $N \to \infty$). However, experimental evidence shows that this is hardly the case. Due to the heterogeneous microstructure of geomaterials, compaction is localized to a thin band of finite thickness (several grains). Consequently, the evolution of the reaction cannot be homogeneous over the REV ($\ell_c \neq 0$, Eq.(26)). For example, assuming, that the REV has a size of $\ell_{REV} = 20$ (twenty grains), then $\ell_c \simeq 4$. The size of the REV is rather a statistical quantity and depends on the material at hand. For the aforementioned characteristic length, the linear stability analysis shows that the perturbation that travels fastest has a wave length equal to approximately $\lambda_{\max} = 160$ grains

(Figure 11) leading to a thickness of 80 grains for the compaction band ($\frac{\lambda_{\max}}{2} = 80 D_0^{50}$) or equivalently to a finite minimum compaction band spacing ($spacing = \lambda_{\max} = L_b / N$ for given $L = L_b$). The derived compaction band thickness refers to the compressive part of the perturbation which is half of the wavelength. For $D_0^{50} = 0.1\text{mm}$ the thickness of the band is 8 mm.

In the literature, field and laboratory observations show that the thickness of deformation bands is variable. Tondi [2007] presents the example of a quite thick compactive shear band of the order of 300 grains. On the contrary, in Baud et al. [2004], the thickness of the compaction band observed is of the order of two grains. In the present analysis the compaction band thickness depends on the chemo-mechanical properties of the material and of the heterogeneity of the microstructure. However, it should be mentioned that the present model should not be considered as predictive and that the calculated compaction band thickness has only a qualitative character. In particular, the derived compaction band thickness corresponds to the thickness of the compacting zone at the onset of the localization. This process zone may decrease further during compaction. For example, strain softening because of grain crushing/fracturing and pore collapse, which was excluded here in order to isolate the effects of dissolution, can decrease further the compaction band thickness. In order to simulate the evolution of the compaction band thickness, a post-bifurcation analysis is necessary which exceeds the scope of the present paper.

The dominant wavelength, $\lambda_{\max}$, depends on the hydraulic diffusivity of the rock. In Figure 12 we trace the Lyapunov exponent, *s*, versus the wavelength λ for different orders of magnitude of the hydraulic diffusivity. The lowest considered value of the dimensionless hydraulic diffusivity c_{hy} is 6×10^{3} and the highest is 6×10^{10}. These values correspond to permeability values ranging from 10^{-13}m^2 to 10^{-20}m^2. Figure 12 shows that a lower permeability of the material leads to a smaller dominant wavelength. In other words, the present model leads to thinner compaction bands for more impermeable materials. From the physical point of view, at the onset of the instability, chemical dissolution leads locally to an abrupt increase of the plastic deformations and an abrupt reduction of the effective vertical stress. In oedometric conditions, this drop of the

586 vertical effective stress leads to a fast increase of the pore pressure inside the compaction band in
587 order to equilibrate the total applied vertical stress, which is assumed constant. Therefore, the role
588 of hydraulic diffusivity is crucial, as a more permeable material would need a larger zone in order
589 for the pore pressure to rapidly increase and equilibrate the constant total vertical stress. On the
590 contrary, in a less permeable material, this zone will be narrower leading to thinner compaction
591 bands. Moreover, the faster the dissolution reaction is, the more rapidly the pore pressure has to
592 build-up in order to equilibrate the total vertical stress. Consequently, for a given value of the
593 hydraulic diffusivity parameter, the chemical softening rate controls the thickness of the
594 localization zone.
595
596 The chemical softening rate depends on the grain damage parameter a and on the dissolution
597 rate k^*. Figure 13 shows the dependency of the compaction band thickness on the grain damage
598 parameter for the numerical example presented in the previous section. As expected, stronger
599 grain damage (i.e. lower values of parameter a) leads to thinner bands (a higher specific surface
600 leads to a higher chemical softening rate). It should be emphasized, though, that this is only a
601 chemical softening effect and that the possible introduction of additional mechanical softening
602 through grain breakage would enhance this trend. Similarly, in Figure 14 we present the
603 dominant wavelength in terms of the grain damage parameter for various orders of magnitude of
604 the dissolution rate coefficient. We observe that a faster reaction rate leads to a narrower
605 compaction band at the onset of the localization. This is due to the fact that higher values of k^*
606 increase the chemical softening rate (Eq.(22) and (23)). Alternatively, the impact of the
607 dissolution rate to strain localization can be investigated through the non-dimensional expression
608 of the hydraulic diffusivity parameter. According to equation (27) by increasing the dissolution
609 rate (faster reaction) the non-dimensional hydraulic diffusivity decreases, which leads to thinner
610 compaction bands as discussed above (Figure 12).
611
612 These mathematical results have to be experimentally verified. In absence of experimental
613 evidence, one could however remark that it is consistent with what is observed for shear bands
614 where the localization zone decreases with increasing mechanical or chemical softening
615 [*Vardoulakis and Sulem*, 1995; *Sulem et al.*, 2011; *Brantut and Sulem*, 2012; *Veveakis et al.*,
616 2012, 2013]. In the present case, the dissolution increases the chemical softening of the material.

617 The deformation rate is linked to the dissolution rate so that a faster dissolution induces a higher
618 softening rate.

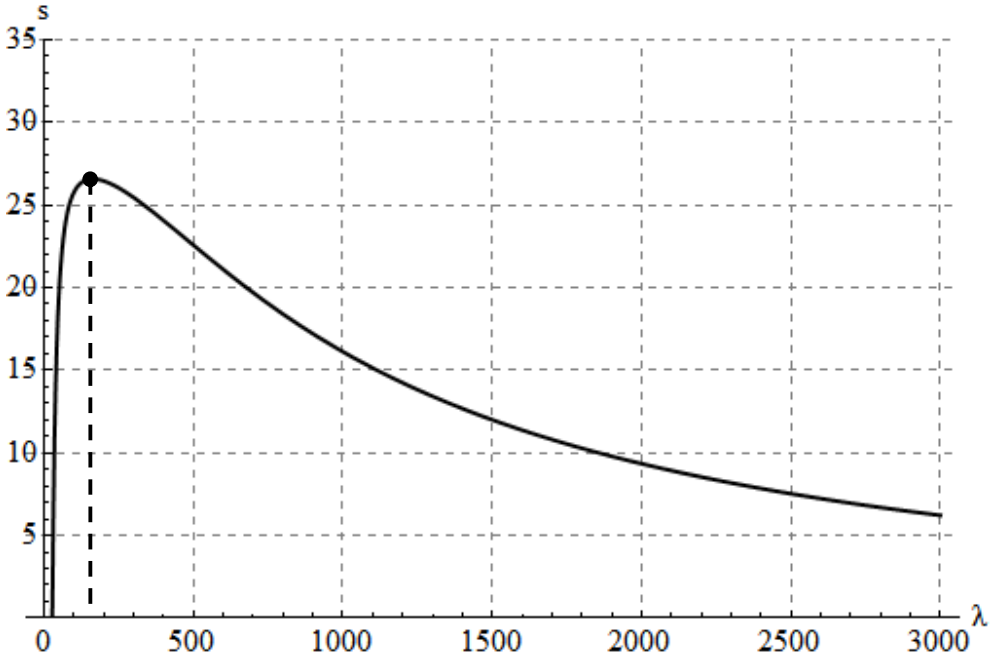

619

620 *Figure 11. Growth coefficient, s, in terms of the perturbation wave length for $a = 10^{-2}$ and*
621 *$\ell_c \simeq 4$. The dominant wave length corresponds to the value of λ for which the growth*
622 *coefficient is maximum. The thickness of the compaction band is proportional to the dominant*
623 *wave length.*

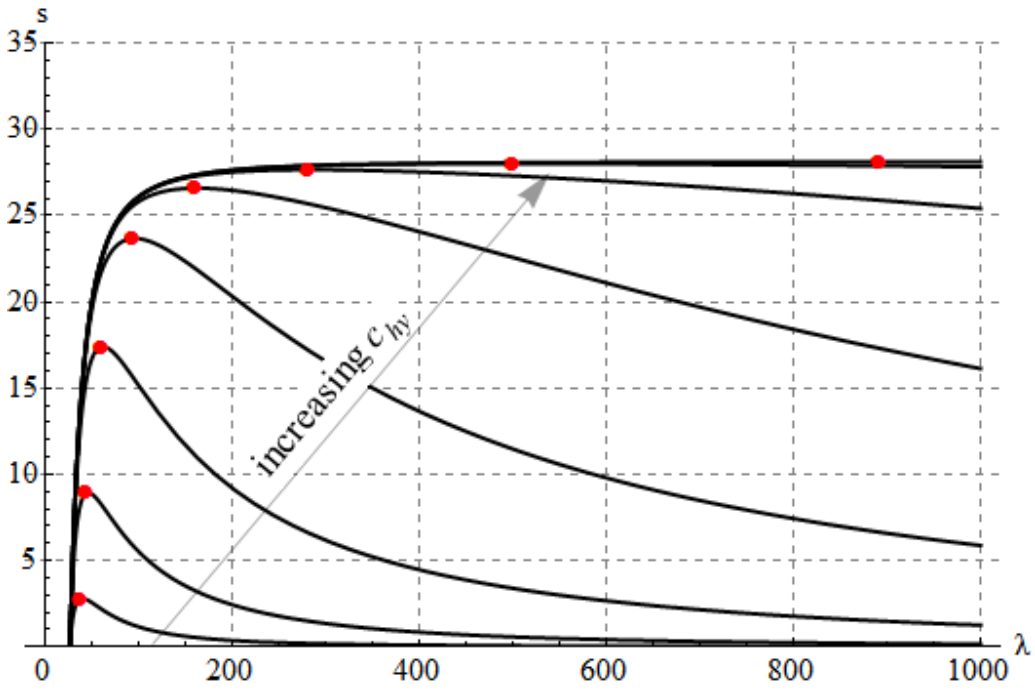

Figure 12. Influence of hydraulic diffusivity on the dominant wavelength for $a = 10^{-2}$ *and* $\ell_c \simeq 4$. *The red dots represent the maximum value of the Lyapunov exponent for a given hydraulic diffusivity. The more impermeable the medium is the more localized the compaction instability becomes (smaller wavelength).*

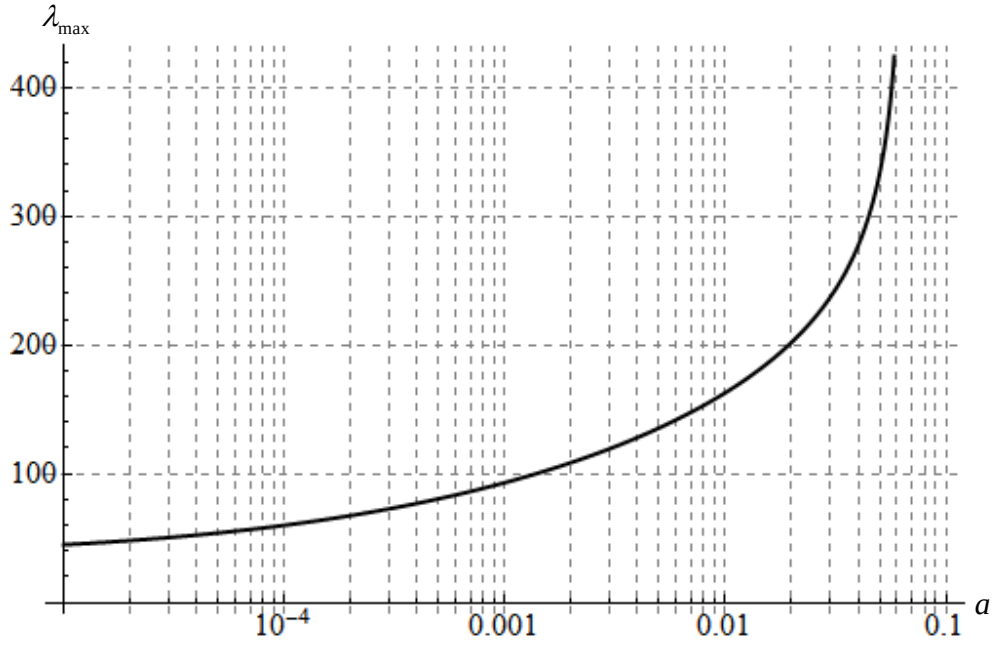

Figure 13. Dominant wave length (wave length selection) in terms of the grain damage parameter a. As the grains become less crushable, λ_{max} tends to infinity and therefore the formation of compaction bands is less likely.

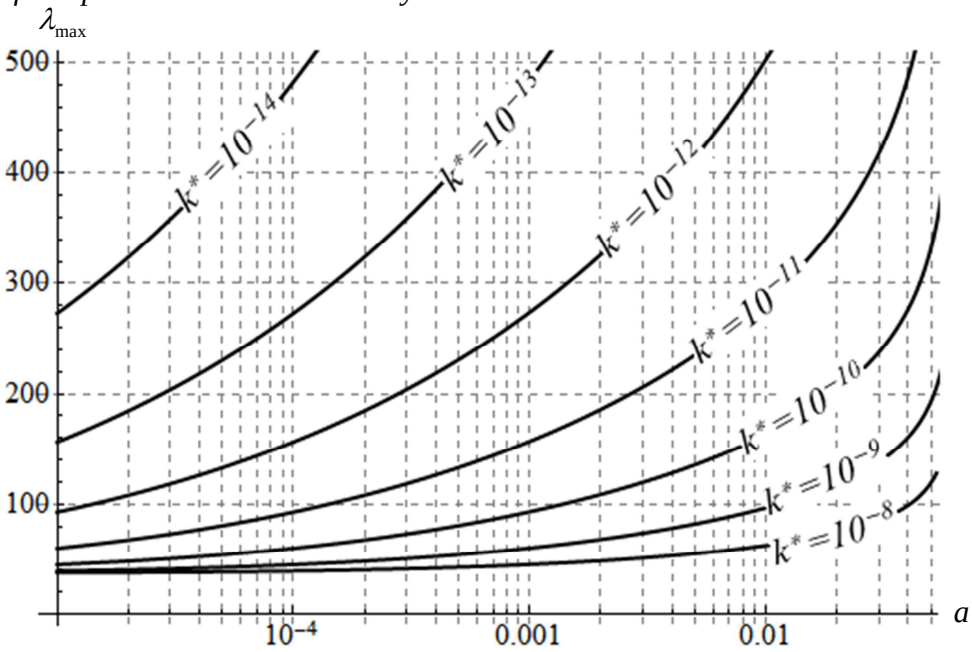

Figure 14. Dominant wave length (wave length selection) in terms of the grain damage parameter a for various values of the dissolution rate (k^* in m/s). The faster the reaction is the narrower the compaction band zone is.

5. Case studies

5.1. Compaction banding of a sandstone reservoir

The scenario of water flooding of a sandstone reservoir at 4km depth is studied in this paragraph. This example could reflect the conditions of enhanced oil recovery by injecting water into the reservoir to maintain the pore pressure. In offshore operations the injected water is commonly seawater, which is different from the formation water. The injection of water can trigger the dissolution of the quartz-based rock (R1) which in turn may trigger compaction band instabilities. At this depth it is assumed that the water pressure is $p_f \simeq 40\text{MPa}$ and the total vertical stress is $\sigma_n \simeq 100\text{MPa}$. Some typical values for sandstone are given in Table 1.

Table 1. Indicative material properties of the sandstone.

Quantity	Value	Dimensionless value
Hydraulic diffusivity, c_{hy}	$2\ 10^{-3}\ \text{m}^2\ \text{s}^{-1}$	$6.25\ 10^{11}$
Grain diameter, D_0^{50}	0.1 mm	1
Effective grain surface area to volume ratio, S	$50\ \text{mm}^{-1}$	1
Bulk modulus, K	10 GPa	100
Shear modulus, G	7.5 GPa	75
Porosity, n	0,20	-
CSL slope, M	1	-
Initial yield stress, p_0'	60 MPa	0.60
Residual yield stress, p_R'	15 MPa	0.15
Chemical Softening exponent, κ	2	-
Grain damage parameter, a	0.5 MPa	0.005
μ_3/μ_2	0,6	-
Fluid density, ρ_f	$1\ \text{g cm}^{-3}$	1
Solid density, ρ_s	$2.65\ \text{g cm}^{-3}$	2.65
Dissolution rate, k	$10^{-8}\ \text{mol s}^{-1}\ \text{m}^{-2}$ ($k^* \simeq 10^{-12}$ m/s)	

Before the reaction takes place the stress state is represented by the point A in the $q-p$ plane (Figure 15). Elastic loading under oedometric conditions is assumed for the initial stress state, i.e.

point A (stress path line no. 1) and $\sigma_{zz} = -\sigma_n = -100\,\text{MPa}$. At time $t = 0$ the reservoir is flooded with water. The water injected in the reservoir is continuously renewed in such a way that practically open flow conditions hold ($w_2(t > 0) = 0$). As a result the system is not in chemical equilibrium and dissolution occurs. Consequently, the material is progressively degraded due to chemical softening and the chemical softening parameter decreases from its initial value $\zeta_0 = 1$. When $\zeta = \zeta_A \simeq 0.9$ the material yields, plastic strains are accumulated and grain damage occurs (Eq.(19)). By neglecting in this phase the influence of the dissolution on the increase of the specific area of the grains of the rock (i.e. effective grain surface area to grain volume ratio, S, is assumed quasi-constant) an estimation of the time needed for yielding is possible. Equations (22) and (23) are combined to give, for sub-spherical grains:

$$t_A \approx \frac{\mu_2}{\mu_3}\frac{\rho_s}{\rho_f}\frac{1}{S k^*}\ln \zeta_A^{-1} \approx 3.5\,\text{months} \tag{46}$$

It should be mentioned that if closed flow conditions were considered ($w_2(t = 0) = 0$, $w_2(t > 0) \neq 0$) then the dissolution would be slower and several injection cycles would be needed for yielding as the solution saturates quite quickly (equilibrium constant: $\log K_{eq} \simeq$ -3.15 at 80°C) without provoking significant chemical softening.

After reaching point A, the yield surface continues to contract due to dissolution and the stress state evolves until point B. At point B the system becomes unstable and compaction band instabilities are triggered. The minimum thickness of the compaction bands is equal to $\pi \ell_c$ (Eq.(42)), but this can be larger depending on the exact stress path, the chemo-mechanical parameters (paragraph 4.4) and the nonlinear behavior of the system in the post bifurcation regime. Contrary to the post bifurcation regime, where the deformations are abruptly localized and the conditions can be considered undrained, drained conditions can be assumed from point A to point B if we consider that the time scale of the pore fluid diffusion is much faster than the time scale of the chemical softening process. Therefore, we can admit that the stress path after yielding follows Path 2 (Figure 15). This path is derived from the fact that the vertical stress is kept constant $\sigma_{zz} = -\sigma_n$ under oedometric conditions (see Eq.(16)).

693 The instability happens when $\zeta = \zeta_B \simeq 0.85$. From point A to point B the specific surface of the
694 grains is smoothly increased as microcracking, debonding and grain crushing take place
695 (homogeneous accumulation of plastic deformations, Eq.(19)). Assuming for simplicity that
696 $S_B \approx S_A$, the time needed for instability ($\zeta_0 \to \zeta_B$) is of the order $t_B \approx 5$ months. After this
697 point the deformations are localized into a zone of finite thickness (Eq.(42)) and excessive grain
698 damage occurs (onset of instability – compaction band formation).
699

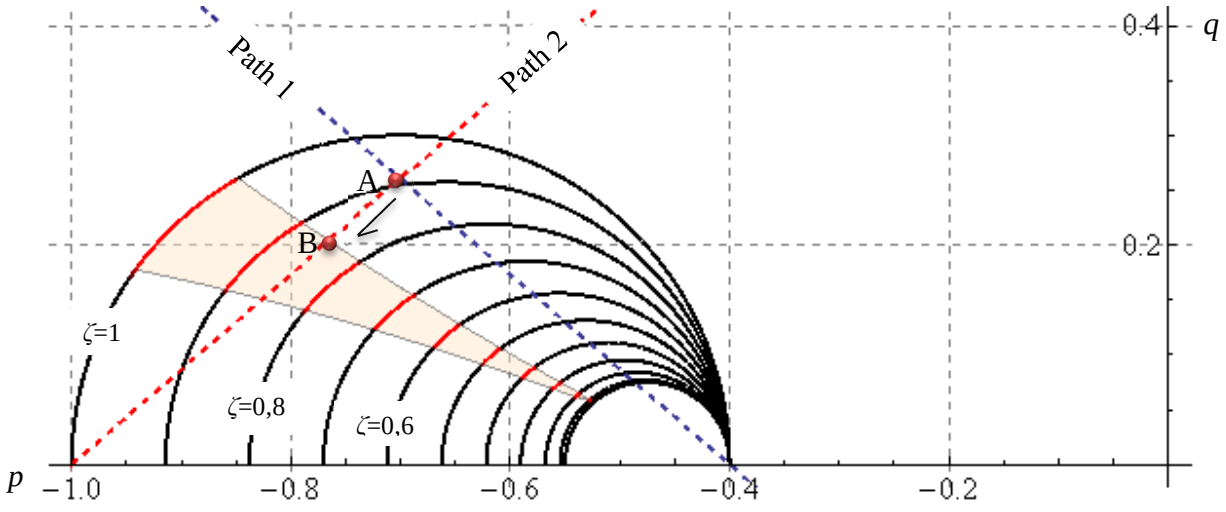

700

701 *Figure 15. Instability region (shaded) for compaction bands under oedometric conditions for a*
702 *sandstone at 4 km depth. Different yield surfaces are drawn for different levels of chemical*
703 *degradation, ζ . The stress path 1 represents the elastic loading of the material under*
704 *oedometric conditions, while the stress path 2 represents the path that the material follows after*
705 *yielding.*

706

707 ***5.2. Compaction banding induced by CO_2 injection in carbonate grainstones***

708 The formation of compaction bands in carbonate rocks is hardly evidenced both in field and in
709 laboratory [*Baud et al.*, 2009]. Nevertheless, more recently, Cilona et al. [2012] observed
710 compaction bands in porous carbonate grainstones both in field and in laboratory. Their
711 observations extend the previous evidence of compaction bands in porous carbonate rocks by
712 Baxevanis et Papamichos [2006] and Tondi et al. [2006]. In the aforementioned works, Hertzian
713 cracks at grain contacts, microcracking, debonding and pore collapse that result in an overall
714 effective grain size reduction were shown to develop inside compaction bands. As it was

mentioned in paragraph 3.2, these mechanisms are essentially taken into account in the proposed model through the hyperbolic fit of the evolution of the effective grain size with the mechanical energy input into the system (Eqs. (18), (19)).

In this paragraph we attempt to explore the possibility of compaction bands formation in carbonate grainstones because of CO_2 injection at 1.8 km depth. The set of reactions that take place because of the CO_2 injection are summarized through the stoichiometry of equation R2. In Table 2 we present some typical values for the chemo-mechanical parameters of a porous carbonate rock. At this depth, we assume that the water pressure is $p_f \simeq 18\text{MPa}$ and the total vertical stress is $\sigma_n \simeq 45\text{MPa}$. The instability region, the elastic and plastic oedometric stress paths as well as the initial stress state (Point A) are shown in Figure 16. Following the same reasoning as in the previous case study, a CO_2 solution is injected in the rock mass. The rock dissolves and its mechanical strength diminishes (open fluid flow conditions). When $\zeta = \zeta_{\text{A}} \simeq 0.9$ the rock starts to yield and a homogeneous plastic strain field is developed. This phase of deformation under constant applied loading (i.e. the overburden) corresponds to the creep behavior that is observed due to CO_2 injection [*Le Guen et al.*, 2007; *Liteanu and Spiers*, 2009; *Rutqvist*, 2012]. At point B (Figure 16), $\zeta = \zeta_{\text{B}} \simeq 0.63$, the system bifurcates and compaction bands are formed. Again the minimum thickness (or spacing) of the compaction bands is equal to $\pi \ell_c$ (Eq.(42)), but this can be different depending on the stress path, the chemo-mechanical parameters and the nonlinear behavior of the system in the post bifurcation regime (mechanical softening).

Under open flow conditions, an estimation for the time needed for reaching point B is $t_{\text{B}} \approx 5\,\text{days}$ (Eq.(46) assuming a constant value for S until the instability and sub-spherical grains). Notice, that this period of time is far smaller as compared to the previous example due to the faster dissolution rate of calcite.

For CO_2, injection open flow conditions would correspond to a zone outside the gas plume where the formation fluid is saturated with CO_2, but is not in chemical equilibrium with the rock so that

744 carbonate dissolution occurs continuously ($w_2 < w_2^{eq}$). Rohmer and Seyedi [2010], using an
745 hydro-mechanical model on a reservoir case study, show that the dissolution front might extend
746 few kilometers around the injection well after 10 years of continuous injection.
747
748 Table 2. Indicative material properties of a carbonate grainstone.

Quantity	Value	Dimensionless value
Hydraulic diffusivity, c_{hy}	10^{-3} m^2 s^{-1}	$3\ 10^5$
Grain diameter, D_0^{50}	0.2 mm	1
Effective grain surface area to volume ratio, S	25 mm^{-1}	1
Bulk modulus, K	5 GPa	110
Shear modulus, G	5 GPa	110
Porosity, n	0.25	-
CSL slope, M	0.9	-
Initial yield stress, p_0'	30 MPa	0.67
Residual yield stress, p_R'	0 MPa	0
Chemical Softening exponent, κ	1	-
Grain crushing parameter, a	1 MPa	0.011
μ_3/μ_2	0.62	-
Fluid density, ρ_f	1 g cm^{-3}	1
Solid density, ρ_s	2.65 g cm^{-3}	2.65
Dissolution rate, k	10^{-6} mol s^{-1} m^{-2} ($k^* \simeq 1.6\ 10^{-10}$ m/s)	

749
750
751
752
753
754
755
756
757
758
759

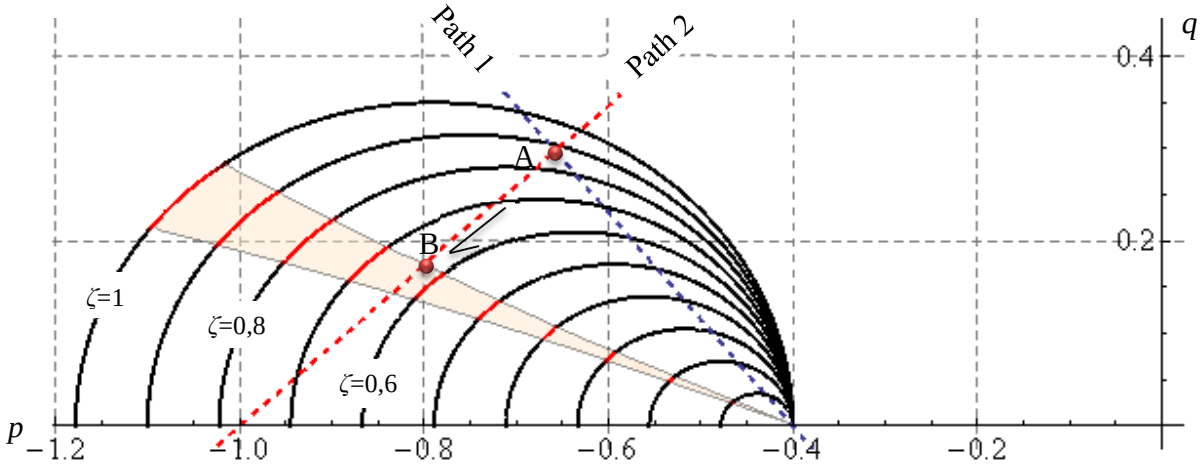

Figure 16. Instability region (shaded) for compaction bands under oedometric conditions for a carbonate grainstone at 1.8 km depth. Different yield surfaces are drawn for different levels of chemical degradation, ζ . The stress path line no. 1 represents the elastic loading of the material under oedometric conditions, while the stress path line no. 2 represents the path that the material follows after yielding.

6. Conclusions

Grain fracturing and attrition, "microcracking" of the cementitious matrix, debonding and pore collapse are some important micro-mechanisms that lead to the reduction of the effective grain size of a geomaterial and consequently to the increase of the dissolution front in reactive environments. The proposed chemo-poro-mechanical model accounts for the aforementioned mechanisms. Part of the mechanical energy supplied to the system is dissipated through various micro-mechanisms for the creation of new surfaces in the microstructure. In this sense, a phenomenological approach based on the work of Lade et al. [1996] is used to relate the effective grain specific surface and the total energy input per specimen unit volume. Following this approach, which describes the above dissipative mechanisms through a single parameter, and in the frame of dissolution process, the chemo-poro-mechanical model presented herein provides a strong coupling between mechanics and reaction kinetics (Figure 1).

The purpose of the present paper was to explore the possibility of chemically induced compaction band instabilities. Therefore, in order to isolate the chemical effects, mechanical softening

induced by grain damage was not considered in the present form of the proposed chemo-poro-mechanical model. The stability of the system is studied through a linear stability analysis, which revealed the critical parameters for which compaction bands may occur in quartz- and carbonate-based rocks. Porosity and grain damage sensitivity (parameter a) are important parameters that considerably influence the triggering of compaction band instabilities due to dissolution. For a specific rock, the determination of the exact value of the grain damage sensitivity parameter is possible and may include classical mechanical tests, grain-size analyses and/or microstructural observations and measurements (e.g. X-ray tomography, acoustic emissions). The other parameters of the model (elastic constants, yield surface, chemical softening factor and reaction kinetics) can also be determined experimentally.

Due to the existing heterogeneity of the microstructure (e.g. different grain sizes and constituents in the REV) the dissolution rate may not be homogeneous over the REV. The size of the REV is a finite statistical quantity that depends upon the geomaterial at hand. Therefore, a rock is characterized by at least one characteristic length, which by appropriately up-scaling the micro-level to the macro-level (separation of scales and averaging) can be adequately expressed at the macroscale, i.e. incorporated into the proposed chemo-poro-mechanical model. The linear stability analysis shows that because of this characteristic length, the deformation is localized into narrow bands of finite thickness and that these bands are periodically distributed in space. This is in accordance with many field and laboratory observations where there is evidence that compaction bands are localized into a thin band (several grains thickness) and are quasi-periodically arranged in space. In field and laboratory observations, the thickness of compaction bands is variable. In the present analysis the compaction band thickness depends on the chemo-poro-mechanical properties of the material and the heterogeneity of the microstructure. According to the present model, the thickness and the periodicity of compaction bands are related to the grain damage parameter, the hydraulic diffusivity and the dissolution rate. The more crushable the grains are, the lower the permeability is and the higher the dissolution rate is, the narrower the compaction band is. Nevertheless, the results presented here have a qualitative character. The study of the precise evolution of the system and of the compaction band thickness after the onset of localization (post-bifurcation regime) exceeds the scope of the present paper

and will be pursued further in a future work by integrating the non-linear chemo-poro-mechanical system of equations.

Finally, two scenarios of chemically induced compaction band instabilities were investigated. The first one concerns the water flooding of a quartzic rock reservoir, while the second one concerns a carbonate grainstone in which a CO_2 solution is injected. The effect of open and closed flow conditions was discussed, the instability regions were determined and a rough estimation of the critical time for compaction band triggering was made. Two phases are distinguished. The first phase is characterized by a creep behavior of the rock, while in the second phase compaction band instabilities are triggered. The present study focused on pure compaction bands, but the concept of the present model can be extended to other types of deformation bands, such as shear bands. The formation of deformation bands in reservoirs due to chemical processes and other non-linearities can be related to important changes in permeability, to the creation of reinforced zones (compactive behavior) or, in the contrary, to the creation of new faults and fractures (shear behavior). However, in order to quantify the implications of such phenomena to the sustainability of reservoir projects, large scale simulations are necessary that will take into account the aforementioned phenomena and the precise injection characteristics.

7. Acknowledgements

The authors would like to acknowledge the associate editor and the anonymous reviewers for their fruitful comments and suggestions, which improved the paper. Moreover, they would like to acknowledge the support of the French National Agency for Research (ANR FISIC n° ANR-11-SEED-0003).

8. Appendix

8.1. Reaction kinetics in terms of mass fraction and specific area

At the microscale the mass fraction is:

838 $$w_2 = \frac{m_2}{m_f} \text{ or } w_2 = \frac{\mu_2}{\rho_f V_f} n_2 \quad \text{(A1)}$$

839 where m_f is the mass of the fluid phase and m_2 is the mass of the dissolution product at the
840 microscale. Assuming that $w_2 \ll 1$ or equivalently that the density of the fluid, ρ_f, remains
841 practically constant during the reaction process, we obtain that:

842 $$\frac{\partial n_2}{\partial t} \approx \frac{\rho_f}{\mu_2} e V_s \frac{\partial w_2}{\partial t} \quad \text{(A2)}$$

843 Furthermore, assuming that the activity coefficients for the reactants are close to unity the
844 reaction quotient is expressed in terms of the reaction activities of the reactants as follows:

845 $$Q \approx \frac{a_2}{a_1} \text{ or } Q \approx \frac{n_2}{n_1} \quad \text{(A3)}$$

846 Assuming again that $w_2 \ll 1$, we obtain:

847 $$Q \approx w_2 \frac{\mu_1}{\mu_2} \quad \text{(A4)}$$

848 Consequently the mass fraction at equilibrium is related to the equilibrium constant as follows:

849 $$w_2^{eq} \approx \frac{\mu_2}{\mu_1} K_{eq} \quad \text{(A5)}$$

850 Using the above expressions, Eq.(20) yields:

851 $$\frac{\partial w_2}{\partial t} \approx k \frac{\mu_2}{\rho_f} \frac{S}{e} \left(1 - \frac{w_2}{w_2^{eq}} \right) \quad \text{(A6)}$$

852 where we set $S = \frac{A}{V_s}$.

8.2. Chemical softening parameter and mass fraction

By definition $\zeta = \frac{M_s}{M_s^0}$ and using the stoichiometry of the dissolution reaction we obtain:

$$\frac{\partial \zeta}{\partial t} = \frac{1}{M_s^0}\frac{\partial M_s}{\partial t} = -\frac{\mu_3}{M_s^0}\frac{\partial n_2}{\partial t} \tag{A7}$$

Using Eq.(A2) at the macroscale (REV) we get for $w_2^M \ll 1$:

$$\frac{\partial \zeta}{\partial t} \approx -\frac{\mu_3}{\mu_2}\frac{M_f}{M_s^0}\frac{\partial w_2^M}{\partial t} = -\frac{\mu_3}{\mu_2}\frac{\rho_f}{\rho_s} e \frac{M_s}{M_s^0}\frac{\partial w_2^M}{\partial t} \tag{A8}$$

or

$$\frac{\partial \zeta}{\partial t} \approx -\frac{\mu_3}{\mu_2}\frac{\rho_f}{\rho_s} e \zeta \frac{\partial w_2^M}{\partial t} \tag{A9}$$

9. References

Aydin, A., and R. Ahmadov (2009), Bed-parallel compaction bands in aeolian sandstone: Their identification, characterization and implications, *Tectonophysics*, *479*(3-4), 277–284, doi:10.1016/j.tecto.2009.08.033.

Baud, P., E. Klein, and T. Wong (2004), Compaction localization in porous sandstones: spatial evolution of damage and acoustic emission activity, *J. Struct. Geol.*, *26*(4), 603–624, doi:10.1016/j.jsg.2003.09.002.

Baud, P., V. Vajdova, and T. Wong (2006), Shear-enhanced compaction and strain localization: Inelastic deformation and constitutive modeling of four porous sandstones, *J. Geophys. Res.*, *111*(B12), 1–17, doi:10.1029/2005JB004101.

Baud, P., S. Vinciguerra, C. David, a. Cavallo, E. Walker, and T. Reuschlé (2009), Compaction and Failure in High Porosity Carbonates: Mechanical Data and Microstructural Observations, *Pure Appl. Geophys.*, *166*(5-7), 869–898, doi:10.1007/s00024-009-0493-2.

875 Baxevanis, T., E. Papamichos, O. Flornes, and I. Larsen (2006), Compaction bands and induced
876 permeability reduction in Tuffeau de Maastricht calcarenite, *Acta Geotech.*, *1*(2), 123–135,
877 doi:10.1007/s11440-006-0011-y.

878 El Bied, A., J. Sulem, and F. Martineau (2002), Microstructure of shear zones in Fontainebleau
879 sandstone, *Int. J. Rock Mech. Min. Sci.*, *39*(7), 917–932, doi:10.1016/S1365-
880 1609(02)00068-0.

881 Bigoni, D., and T. Hueckel (1991), Uniqueness and localization—I. Associative and non-
882 associative elastoplasticity, *Int. J. Solids Struct.*, *28*(2), 197–213, doi:10.1016/0020-
883 7683(91)90205-T.

884 Brantut, N., and J. Sulem (2012), Strain Localization and Slip Instability in a Strain-Rate
885 Hardening, Chemically Weakening Material, *J. Appl. Mech.*, *79*(3), 031004,
886 doi:10.1115/1.4005880.

887 Brantut, N., M. J. Heap, P. G. Meredith, and P. Baud (2013), Time-dependent cracking and brittle
888 creep in crustal rocks: A review, *J. Struct. Geol.*, *52*, 17–43, doi:10.1016/j.jsg.2013.03.007.

889 Castellanza, R., and R. Nova (2004), Oedometric Tests on Artificially Weathered Carbonatic Soft
890 Rocks, *J. Geotech. Geoenvironmental Eng.*, *130*(7), 728–739, doi:10.1061/(ASCE)1090-
891 0241(2004)130:7(728).

892 Cheung, C. S. N., P. Baud, and T. Wong (2012), Effect of grain size distribution on the
893 development of compaction localization in porous sandstone, *Geophys. Res. Lett.*, *39*(21),
894 n/a–n/a, doi:10.1029/2012GL053739.

895 Cilona, A., P. Baud, E. Tondi, F. Agosta, S. Vinciguerra, A. Rustichelli, and C. J. Spiers (2012),
896 Deformation bands in porous carbonate grainstones: Field and laboratory observations, *J.*
897 *Struct. Geol.*, *45*, 137–157, doi:10.1016/j.jsg.2012.04.012.

898 Coussy, O. (2004), *Poromechanics*, Wiley.

899 Croizet, D., F. Renard, and J.-P. Gratier (2013), Compaction and porosity reduction in
900 carbonates: A review of observations, theory, and experiments, *Adv. Geophys.*, *54*, 181–238,
901 doi:10.1016/B978-0-12-380940-7.00003-2.

902 Cubillas, P., S. Köhler, M. Prieto, C. Chaïrat, and E. H. Oelkers (2005), Experimental
903 determination of the dissolution rates of calcite, aragonite, and bivalves, *Chem. Geol.*,
904 *216*(1-2), 59–77, doi:10.1016/j.chemgeo.2004.11.009.

905 Das, A., G. D. Nguyen, and I. Einav (2011), Compaction bands due to grain crushing in porous
906 rocks: A theoretical approach based on breakage mechanics, *J. Geophys. Res.*, *116*(B8), 1–
907 14, doi:10.1029/2011JB008265.

908 Ghabezloo, S., and J. Sulem (2008), Stress dependent thermal pressurization of a fluid-saturated
909 rock, *Rock Mech. Rock Eng.*, *42*(1), 1–24, doi:10.1007/s00603-008-0165-z.

910 Grgic, D. (2011), Influence of CO 2 on the long-term chemomechanical behavior of an oolitic
911 limestone, *J. Geophys. Res.*, *116*(B7), B07201, doi:10.1029/2010JB008176.

912 Le Guen, Y., F. Renard, R. Hellmann, E. Brosse, M. Collombet, D. Tisserand, and J.-P. Gratier
913 (2007), Enhanced deformation of limestone and sandstone in the presence of high P co 2
914 fluids, *J. Geophys. Res.*, *112*(B5), B05421, doi:10.1029/2006JB004637.

915 Holcomb, D., J. W. Rudnicki, K. a. Issen, and K. Sternlof (2007), Compaction localization in the
916 Earth and the laboratory: state of the research and research directions, *Acta Geotech.*, *2*(1),
917 1–15, doi:10.1007/s11440-007-0027-y.

918 Hu, L. B., and T. Hueckel (2007a), Coupled chemo-mechanics of intergranular contact: Toward a
919 three-scale model, *Computers and Geotechnics*, *34*(4), 306–327,
920 doi:10.1016/j.compgeo.2007.02.009.

921 Hu, L. B., and T. Hueckel (2007b), Creep of saturated materials as a chemically enhanced rate-
922 dependent damage process, *Int. J. Numer. Anal. Methods Geomech.*, *31*(14), 1537–1565,
923 doi:10.1002/nag.600.

924 Issen, K. a., and J. W. Rudnicki (2000), Conditions for compaction bands in porous rock, *J.*
925 *Geophys. Res.*, *105*(B9), 21529, doi:10.1029/2000JB900185.

926 Katsman, R., and E. Aharonov (2006), A study of compaction bands originating from cracks,
927 notches, and compacted defects, *J. Struct. Geol.*, *28*(3), 508–518,
928 doi:10.1016/j.jsg.2005.12.007.

929 Katsman, R., E. Aharonov, and H. Scher (2005), Numerical simulation of compaction bands in
930 high-porosity sedimentary rock, *Mech. Mater.*, *37*(1), 143–162,
931 doi:10.1016/j.mechmat.2004.01.004.

932 Lade, P. V., J. A. Yamamuro, and P. A. Bopp (1996), Significance of Particle Crushing in
933 Granular Materials, *J. Geotech. Eng.*, *122*(4), 309–316, doi:10.1061/(ASCE)0733-
934 9410(1996)122:4(309).

935 Liteanu, E., and C. J. Spiers (2009), Influence of pore fluid salt content on compaction creep of
936 calcite aggregates in the presence of supercritical CO2, *Chem. Geol.*, *265*(1-2), 134–147,
937 doi:10.1016/j.chemgeo.2008.12.010.

938 Marketos, G., and M. D. Bolton (2009), Compaction bands simulated in Discrete Element
939 Models, *J. Struct. Geol.*, *31*(5), 479–490, doi:10.1016/j.jsg.2009.03.002.

940 Nova, R., R. Castellanza, and C. Tamagnini (2003), A constitutive model for bonded
941 geomaterials subject to mechanical and/or chemical degradation, *Int. J. Numer. Anal.*
942 *Methods Geomech.*, *27*(9), 705–732, doi:10.1002/nag.294.

943 Olsson, W. A., D. J. Holcomb, and J. W. Rudnicki (2002), Compaction Localization in Porous
944 Sandstone: Implications for Reservoir Mechanics, *Oil Gas Sci. Technol.*, *57*(5), 591–599,
945 doi:10.2516/ogst:2002040.

946 Rice, J. R. (1976), The localization of plastic deformation, in *Theoretical and Applied Mechanics*
947 *(Proceedings of the 14th International Congress on Theoretical and Applied Mechanics)*,
948 edited by W. T. Koiter, pp. 207–220, NorthHolland Publishing Co., Delft.

949 Rimstidt, J. D., and H. L. Barnes (1980), The kinetics of silica-water reactions, *Geochim.*
950 *Cosmochim. Acta*, *44*(11), 1683–1699, doi:10.1016/0016-7037(80)90220-3.

951 Rohmer, J., and D. M. Seyedi (2010), Coupled Large Scale Hydromechanical Modelling for
952 Caprock Failure Risk Assessment of CO 2 Storage in Deep Saline Aquifers, *Oil Gas Sci.*
953 *Technol. – Rev. l'Institut Français du Pétrole*, *65*(3), 503–517, doi:10.2516/ogst/2009049.

954 Rudnicki, J. W. (2002), Diffusive instabilities in dilating and compacting geomaterials, in
955 *Multiscale Deformation and Fracture in Materials and Structures, Solid Mechanics and Its*
956 *Applications, Volume 84*, Kluwer Academic Publishers.

957 Rudnicki, J. W., and J. R. Rice (1975), Conditions for the localization of deformation in pressure-
958 sensitive dilatant materials, *J. Mech. Phys. Solids*, *23*(6), 371–394, doi:10.1016/0022-
959 5096(75)90001-0.

960 Rustichelli, A., E. Tondi, F. Agosta, A. Cilona, and M. Giorgioni (2012), Development and
961 distribution of bed-parallel compaction bands and pressure solution seams in carbonates
962 (Bolognano Formation, Majella Mountain, Italy), *J. Struct. Geol.*, *37*, 181–199,
963 doi:10.1016/j.jsg.2012.01.007.

964 Rutqvist, J. (2012), The Geomechanics of CO2 Storage in Deep Sedimentary Formations,
965 *Geotech. Geol. Eng.*, *30*(3), 525–551, doi:10.1007/s10706-011-9491-0.

966 Rutter, E. H. (1983), Pressure solution in nature, theory and experiment, *J. Geol. Soc. London.*,
967 *140*(5), 725–740, doi:10.1144/gsjgs.140.5.0725.

968 Shin, H. (2009), Development of discontinuities in granular media, Georgia Institute of
969 Technology.

970 Shin, H., and J. C. Santamarina (2009), Mineral Dissolution and the Evolution of k0, *J. Geotech.*
971 *Geoenvironmental Eng.*, *135*(8), 1141–1147, doi:10.1061/(ASCE)GT.1943-5606.0000053.

972 Stefanou, I., and J. Sulem (2013), Chemical degradation and compaction instabilities in
973 geomaterials, in *5th BIOT Conference on Poromechanics*, vol. 33, Vienne.

974 Sternlof, K. R., J. W. Rudnicki, and D. D. Pollard (2005), Anticrack inclusion model for
975 compaction bands in sandstone, *J. Geophys. Res.*, *110*(B11), 1–16,
976 doi:10.1029/2005JB003764.

977 Sulem, J., and H. Ouffroukh (2006), Shear banding in drained and undrained triaxial tests on a
978 saturated sandstone: Porosity and permeability evolution, *Int. J. Rock Mech. Min. Sci.*,
979 *43*(2), 292–310, doi:10.1016/j.ijrmms.2005.07.001.

980 Sulem, J., I. Stefanou, and E. Veveakis (2011), Stability analysis of undrained adiabatic shearing
981 of a rock layer with Cosserat microstructure, *Granul. Matter*, *13*(3), 261–268,
982 doi:10.1007/s10035-010-0244-1.

983 Tondi, E. (2007), Nucleation, development and petrophysical properties of faults in carbonate
984 grainstones: Evidence from the San Vito Lo Capo peninsula (Sicily, Italy), *J. Struct. Geol.*,
985 *29*(4), 614–628, doi:10.1016/j.jsg.2006.11.006.

986 Tondi, E., M. Antonellini, A. Aydin, L. Marchegiani, and G. Cello (2006), The role of
987 deformation bands, stylolites and sheared stylolites in fault development in carbonate
988 grainstones of Majella Mountain, Italy, *J. Struct. Geol.*, *28*(3), 376–391,
989 doi:10.1016/j.jsg.2005.12.001.

990 Tran, M. K., H. Shin, Y.-H. Byun, and J.-S. Lee (2012), Mineral dissolution effects on
991 mechanical strength, *Eng. Geol.*, *125*, 26–34, doi:10.1016/j.enggeo.2011.10.014.

992 Vardoulakis, I., and J. Sulem (1995), *Bifurcation Analysis in Geomechanics*, Blackie, Glascow.

993 Veveakis, E., J. Sulem, and I. Stefanou (2012), Modeling of fault gouges with Cosserat
994 Continuum Mechanics: Influence of thermal pressurization and chemical decomposition as
995 coseismic weakening mechanisms, *J. Struct. Geol.*, *38*, 254–264,
996 doi:10.1016/j.jsg.2011.09.012.

997 Veveakis, M., I. Stefanou, and J. Sulem (2013), Failure in shear bands for granular materials:
998 thermo-hydro-chemo-mechanical effects, *Géotechnique Lett.*, *3*(April-June), 31–36,
999 doi:10.1680/geolett.12.00063.

1000 Walsh, J. B., and W. F. Brace (1984), The effect of pressure on porosity and the transport
1001 properties of rock, *J. Geophys. Res.*, *89*(B11), 9425, doi:10.1029/JB089iB11p09425.

1002 Wang, B., Y. Chen, and T. Wong (2008), A discrete element model for the development of
1003 compaction localization in granular rock, *J. Geophys. Res.*, *113*(B3), B03202,
1004 doi:10.1029/2006JB004501.

1005 Wong, T., and P. Baud (2012), The brittle-ductile transition in porous rock: A review, *J. Struct.*
1006 *Geol.*, *44*, 25–53, doi:10.1016/j.jsg.2012.07.010.

1007 Xie, S. Y., J. F. Shao, and W. Y. Xu (2011), Influences of chemical degradation on mechanical
1008 behaviour of a limestone, *Int. J. Rock Mech. Min. Sci.*, *48*(5), 741–747,
1009 doi:10.1016/j.ijrmms.2011.04.015.

1010 Zhu, W., P. Baud, and T. Wong (2010), Micromechanics of cataclastic pore collapse in
1011 limestone, *J. Geophys. Res.*, *115*(B4), B04405, doi:10.1029/2009JB006610.

1012 Zinsmeister, L., J. Dautriat, A. Dimanov, J. Raphanel, and M. Bornert (2013), Mechanical
1013 evolution of an altered limestone using 2D and 3D digital image correlation (DIC), in *47th*
1014 *U.S. Rock Mechanics / Geomechanics Symposium*, San Francisco, CA, USA.

1015

1016

1017

List of Captions

1073